Session 2P5
Electromagnetic Modeling and Inversion and Applications 1

New GL Method and Its Advantages for Resolving Historical Difficulties

G. Xie, F. Xie, and J. Li
GL Geophysical Laboratory, USA

Abstract—In this paper, we propose two types of new electromagnetic (EM) integral equation systems and their dual integral equation systems. Based on the EM integral equation systems, we propose the new GL EM modeling and inversion algorithms. Abstracts of our GL EM method based on the magnetic differential integral equation and the electrical integral differential equation have been published in PIERS 2005 in Hangzhuo. We used finite step iterations to exactly solve these integral equation systems or the EM and seismic differential integral equations in finite sub domains. The Global EM wave field is improved successively by the Local scattering EM wave field in the sub domains. In the FEM and FD method, the large matrix equation, inaccurate and complex absorption condition on artificial boundary, the cylindrical and spherical coordinate singularities, and ill posed in inversion are historical difficulties. The Born approximation is only used for low contrast material. The GL method is completely different from FEM, FD, and Born approximation. Our GL modeling and inversion resolved these historical difficulties. Only 3×3 or 6×6 small matrices need to be solved in the GL method; There is no artificial boundary for infinite domain in the GL method; In the GL method, the cylindrical and spherical coordinate singularities are resolved; Our GL method combines the analytic and asymptotic method and numerical method perfectly. It is more accurate than FEM and FD method and Born likes approximation. The GL method is available for all frequencies and high contrast materials. The GL solution has $O(h^2)$ convergent rate. If the Gaussian integrals are used, the GL field has $O(h^4)$ super convergence. The GL method is a high perform parallel algorithm with intrinsic self parallelization properties. The FEM and FD scheme of high order PDE are complicated. Fortunately, the GL method has very simple scheme or no scheme or half scheme such that it has half mesh and no mesh. The FEM and FD scheme only used Riemann integral. In the GL method, we can use both of Riemann and Lebesgue integral that induces a meshless method. We have developed software for 3D/2.5D EM, seismic, acoustic, flow dynamic, and QEM modeling and inversion. Our GL modeling and inversion are useful for geophysical and Earthquake exploration, environment engineering, nondestructive testing, steel and metal casting, weather radar, medical, Earth magnetic, antenna, and heating conductive imaging, space sciences and lunar and sun and stars EM and light exploration. The GL QEM modeling and inversion can be useful for studying micro optical physical and biophysical properties in nanometer materials and biophysics materials. The GL and AGILD method resolved the singularity difficulties at the poles in Navier-Stocks flow atmosphere simulation and Earth and Space EM field. We find GL numerical quanta for very high frequency EM field by GL simulation.

1. Introduction

The existing EM theory and analytical and numerical methods are published in many books and journals. However, there are historical difficulties in EM and other field modeling and inversion. The large matrix equation, inaccurate and complex absorption conditions on artificial boundary, the cylindrical and spherical coordinate singularities, and ill posed in the modeling and inversion are historical difficulties. The Born approximation can be only used for low contrast material. In this paper, we propose a new GL method "Global and Local field modeling and inversion" for resolving these historical difficulties. Our GL method is completely different from the FEM, FD, Born approximation methods.

We consider the EM, seismic, acoustic, quantum, flow and other field equations on finite inhomogeneous domain that is imbedded into an infinite domain. The analytical incident field and Green field in the background domain are called an initial global field. The inhomogeneous domain is divided into mesh or meshless sub domains. The global field is changing by local scattering field successively in each sub domain. The GL method processes will be finished when the Global field is passing through the all Local sub domains with inhomogeneous material. First in the world, the abstracts of our GL method have been published in Piers 2005 in Hangzhuo. [1, 4–9], and in the GL Geophysical Laboratorys reports [2–3].

The new GL method has the following advantages: (1) There is no large matrix to solve, only 3×3 or 6×6 small matrices need to be solved; (2) There is no artificial boundary for infinite domain; (3) The GL method combines the analytic and asymptotic method and numerical method consistently. It is more accurate than FEM and FD method and Born likes approximation; (4) The GL modeling solution has $O(h^2)$ convergent rate. In particular, if the Gaussian integrals are used, the GL solution has $O(h^4)$ super convergence; (5) The cylindrical and spherical coordinate singularities are resolved; (6) It is available for all frequencies and high contrast materials; (7) the GL method has very simple or no scheme, it has half mesh or no mesh; (8) In the GL method, we can use both Riemann and Lebesgue integrals that induce meshless methods; (9) GL method can couple consistently with AGILD, FEM, and FD method; (10) The GL method is an intrinsic self parallel algorithm in parallel T3E and PC cluster.

The plan of this paper is as follows: The introduction is presented in the section 1. In the section 2, we propose the EM integral equation systems. We propose the 3D/2D GL EM modeling based on the EM integral equation system in the section 3. In section 4, we propose the 3D/2D GL EM modeling based on the EM differential integral equation and electric and magnetic field integral equations. We propose the GL EM inversion in the section 5. In section 6, we prove the fundamental theorems of the GL method. We describe advantages of the GL method in the section 7. The GL software, applications and conclusions are described in the section 8.

2. New Electromagnetic Integral Equation Systems

In this section, we propose the new EM integral equation systems as follows:

$$\begin{bmatrix} E(r) \\ H(r) \end{bmatrix} = \begin{bmatrix} E_b(r) \\ H_b(r) \end{bmatrix} + \int\limits_{\Omega} \begin{bmatrix} E_b^J(r',r) & H_b^J(r',r) \\ E_b^M(r',r) & H_b^M(r',r) \end{bmatrix} [D] \begin{bmatrix} E(r') \\ H(r') \end{bmatrix} dr', \tag{1}$$

$$\begin{bmatrix} E(r) \\ H(r) \end{bmatrix} = \begin{bmatrix} E_b(r) \\ H_b(r) \end{bmatrix} + \int\limits_{\Omega} \begin{bmatrix} E^J(r',r) & H^J(r',r) \\ E^M(r',r) & H^M(r',r) \end{bmatrix} [D] \begin{bmatrix} E_b(r') \\ H_b(r') \end{bmatrix} dr', \tag{2}$$

where [D] is the EM material parameter variation matrix, for the isotropy materials, [D] is 6×6 diagonal matrix with variance materials $(\sigma + i\omega\varepsilon) - (\sigma_b + i\omega\varepsilon_b)$ and $i\omega(\mu - \mu_b)$, for anisotropy materials the [D] will be 6×6 full matrix. $E(r)$ is the electric field, $H(r)$ is the magnetic field, $E_b(r)$ is incident electric field in the background medium, $H_b(r)$ is incident magnetic field in the background medium, $E_b^M(r',r), \ldots, H_b^M(r',r)$ are electric or magnetic background field Green tensors exciting by the electric or magnetic dipole source respectively, The integral equations (1) and (2) are the dual system of each other.

3. The 3D/2D New GL EM Modeling Based on the Electromagnetic Integral Equation System

We propose the GL EM modeling based on the EM integral equation system in this section.

(3.1) The domain Ω is divided into a set of n mesh or meshless sub domains $\{\Omega_k\}$, $\Omega = \bigcup\{\Omega_k\}$.

(3.2) In each Ω_k, we solve the EM Green tensor integral equation system based on the equations (1) and (2). By dual curl operation, the equation systems are reduced into a 6×6 matrix equations. By solving the 6×6 equations, we obtain Green tensor field E_k^J and H_k^M.

(3.3) We improve the Global EM field $[E_k(r), H_k(r)]$ by the Local scattering field

$$\begin{bmatrix} E(r) \\ H(r) \end{bmatrix}_k = \begin{bmatrix} E(r) \\ H(r) \end{bmatrix}_{k-1} + \int\limits_{\Omega_k} \begin{bmatrix} E_k^J(r',r) & H_k^J(r',r) \\ E_k^M(r',r) & H_k^M(r',r) \end{bmatrix} [D] \begin{bmatrix} E(r') \\ H(r') \end{bmatrix}_{k-1} dr', \tag{3}$$

$k = 1, 2, \ldots n$, successively. The $[E_n(r), H_n(r)]$ is the GL solution of the EM integral equations (1) and (2).

4. The 3D/2D GL EM Modeling Based on the EM Differential Integral Equation

4.1. The GL EM Modeling Based on the Magnetic Differential Integral Equation

Since 1995, we have proposed the magnetic field differential integral equation (MDI) in the frequency and time domain [10-13]. In this section, we propose the dual magnetic field differential integral equation of our MDI [10-13],

$$H(r) = H_b(r) + \int\limits_{\Omega} \frac{(\sigma + i\omega\varepsilon) - (\sigma_b + i\omega\varepsilon_b)}{\sigma + i\omega\varepsilon} E^M(r',r) \cdot \nabla \times H_b(r') dr'. \tag{4}$$

Based on the equation (4), the GL magnetic field modeling is as follows:

(4.1) The step (4.1) is the same as (3.1).

(4.2) In each Ω_k, $k = 1, 2, \dots n$, we solve the magnetic field differential integral equation to find $E_k^M(r', r)$ successively. By the dual curl operation, only 3×3 matrix equations need to be solved.

(4.3) We improve the Global EM field $H_k(r)$ by the Local scattering field

$$H_k(r) = H_{k-1}(r) + \int\limits_{\Omega_k} \frac{(\sigma + i\omega\varepsilon) - (\sigma_b + i\omega\varepsilon_b)}{\sigma + i\omega\varepsilon} E_k^M(r', r) \cdot \nabla \times H_{k-1}(r') dr', \tag{5}$$

$k = 1, 2, \dots n$, successively. $H_n(r)$ is the GL magnetic field solution of (4).

4.2. GL EM Modeling Based on the Electric Differential Integral Equation

We propose the GL electric field modeling based on the dual electric field differential integral equation of our EDI in 1995[10-13],

$$E(r) = E_b(r) + \int\limits_{\Omega} \frac{\mu - \mu_b}{\mu} H^J(r', r) \cdot \nabla \times E_b(r') dr'. \tag{6}$$

4.3. GL EM Modeling Based on the Electric and Magnetic Integral Equation

We propose the GL method based on the electric integral equation and the magnetic integral equation. Since the electric and magnetic integral equations have divergent Green kernel, a special approach for resolving the divergent singularity is developed.

4.4. GL Modeling for Quantum Field and QEM Field

We propose the GL Schordinger modeling for two hydrogen atoms and interaction between QEM field and atoms that is useful for QEM field in nanometer materials. We find GL numerical quanta for very high frequency EM field by GLQEM simulation.

5. The New GL EM Inversion

The formal logic system and experiments are base of the sciences. Most equations are forward equations. Maxwell equation and elastic equation are forward equation and are not for inversion. The EM integral equation systems (1) and (2) and equations (4) and (6) can be used for both forward and inversion. They are well posed for forward and ill posed for inversion. From essential formal logic in physics, these equations are well posed for forward and ill posed for inversion. How to build a well posed inverse equation is the main project of scientific inversion. Our new idea of the inverse formal logic and inverse experiment in physics motivates us to propose the GL inversion that is a new explicit inversion.

5.1. The GL EM Inversion GLEMI1 for Determining $\boldsymbol{\sigma}$, $\boldsymbol{\varepsilon}$, and $\boldsymbol{\mu}$

The following EM integral equation is for increments of EM parameters $\delta\sigma$, $\delta\varepsilon$, $\delta\mu$,

$$\begin{bmatrix} \delta E(r) \\ \delta H(r) \end{bmatrix}_k = \int\limits_{\Omega_k} \begin{bmatrix} E_k^J(r', r) & H_k^J(r', r) \\ E_k^M(r', r) & H_k^M(r', r) \end{bmatrix} [\delta D]_k \begin{bmatrix} E(r') \\ H(r') \end{bmatrix}_{k-1} dr'. \tag{7}$$

5.2. The GL EM Inversion GLEMI2 for Determining $\boldsymbol{\sigma}$, $\boldsymbol{\varepsilon}$

The following magnetic field differential integral equation is for increments of parameters $\delta\sigma$, $\delta\varepsilon$,

$$\delta H_k(r) = -\int\limits_{\Omega_k} \frac{(\delta\sigma + i\omega\delta\varepsilon)}{(\sigma + i\omega\varepsilon)^2} E_k^M(r', r) \cdot \nabla \times H_{k-1}(r') dr'. \tag{8}$$

5.3. The GL EM Inversion GLEMI3 for Determining $\boldsymbol{\mu}$

The following electric field differential integral equation is for increment of EM parameter $\delta\mu$,

$$\delta E_k(r) = -\int\limits_{\Omega_k} \frac{\delta\mu}{\mu^2} H_k^M(r', r) \cdot \nabla \times E_{k-1}(r') dr'. \tag{9}$$

The suitable strong and weaker regularizing should be added to (7), (8), and (9) to control inversion being stable and reasonable resolution. In our GL EM inversion, only smaller matrices need to be solved. The resolution is dependent on the data configuration, quality and the regularizing parameter.

6. The Fundamental Theorems of the GL Method

Theorem 1. The GL EM field $[E_n(r), H_n(r)]$ from (3.1)–(3.3) is convergent to exact EM field that satisfies the EM integral equation systems (1) and (2). The GL EM field $[E_n(r), H_n(r)]$ is convergent to exact EM field that satisfies the MAXWELL EM equation in 3D or 2D.

Theorem 2. The GL Magnetic field, $H_n(r)$ from (4.1)–(4.3) is convergent to the exact magnetic field, $H(r)$ that satisfies the magnetic field differential integral equation (4). The GL EM field, $H_n(r)$ is convergent to the exact magnetic field $H(r)$ that satisfies the exact MAXWELL EM equation.

Theorem 3. By Riemann division, the GL EM field $[E_n(r), H_n(r)]$ from (3.1–3.3) and the GL magnetic field $H_n(r)$ from (4.1–4.3) have $O(h^2)$ convergent if the trapezoid and mid point integrals are used. In particular, if the Gaussian integrals are used, the GL EM field has $O(h^4)$ super convergent rate. Proof: The theorem 1–3 have proved in [2].

7. Advantages of the GL Method

We have summarized the advantages of the GL method in the introduction. By reviewing the GL modeling and inversion in section 3, 4, and 5, we present several advantages as follows. We consider EM modeling in infinite domain that involves the finite inhomogeneous boundary domain. When we use FEM or implicit FD method to solve the problem, we need the radiation or absorption boundary condition on the artificial boundary with large enough domain. Solving the large matrix is difficult. The radiation and absorption boundary condition is complicated and inconvenience. In the EM inversion, the FEM and FD EM modeling is used in iterations. The absorption boundary errors will propagate into the internal domain, the noise is enhancing to damage the inversion. In the section 2, we propose the EM integral equation systems (1) and (2) that are equivalent to the 3D and 2.5D Maxwell EM equation in infinite domain with finite inhomogeneous domain for isotropic and anisotropic materials. Our GL EM modeling does not need any artificial boundary for solving the EM integral equation and the magnetic differential integral equation. Our GL EM modeling only needs to solve 3×3 or 6×6 small matrices, it does not need to solve any large matrix. There are $1/\rho^2$ singularity in the cylindrical coordinate and $1/r^2$, $1/\sin^2\phi$ singularities in the spherical coordinate system for Maxwell equation. These coordinate singularities are historic difficulties in FEM and FD method. In the EM integral equations (1–3) and electric and magnetic differential integral equations (4–6) for the cylindrical and spherical coordinate, the coordinate singularities are resolved. There is no coordinate singularity in the GL method. The GL modeling combines analytical and numerical methods consistent together and has super convergence. The GL method resolve many historical difficulties in traditional FEM, FD, and Bron approximation methods.

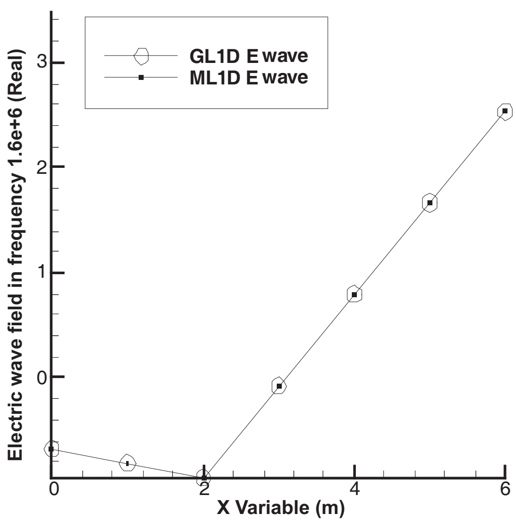

Figure 1: GL and ML Electric wave with freq. $1.6e^6$ Hz

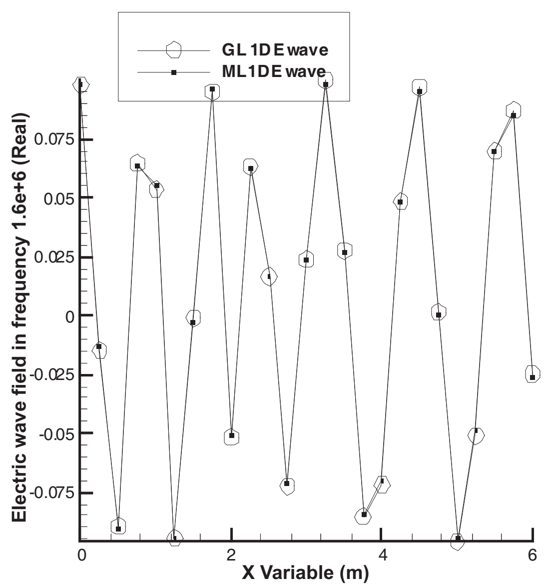

Figure 2: GL and ML Electric wave with freq. $1.6e^8$ Hz

We have created the GL method Since 2002. We have developed the seismic, EM, acoustic, flow, and Quantum field GL modeling and inversion algorithms and software. Many simulations show that the GL seismic and EM wave field has no any boundary error reflection. We have made several GL seismic and EM wave propagation movies that show the wave excited by internal sources is out going propagation perfectly without any error reflection on the boundary. Because the page limitation, we only use one dimension wave propagation to compare GL method and FEM method in the frequency domain. The absorption boundary condition is used for FEM. The numerical results show that GL wave is very accurate to match the multiple layer analytic wave for the high frequency 1.6×10^6 (Figure 1) and frequency 1.6×10^8 (Figure 2). The Figures 3 and 4 show that the FEM is fail to approximate the exact wave in the high Frequency. Our GL method and AGILD method have used in the EM stirring magnetic field simulation and obtained very accurate EM field. The GL, ML, and FEM total and scattering electric wave are shown in Figure 5 and figure 6 respectively. They show that the GL electric wave is very accurate to match to multiple layer wave, but FEM wave is not. Many 2.5D and 3D GL EM and seismic Wave show that GL modeling is accurate, fast and stable. The GL inversion is reasonable high resolution.

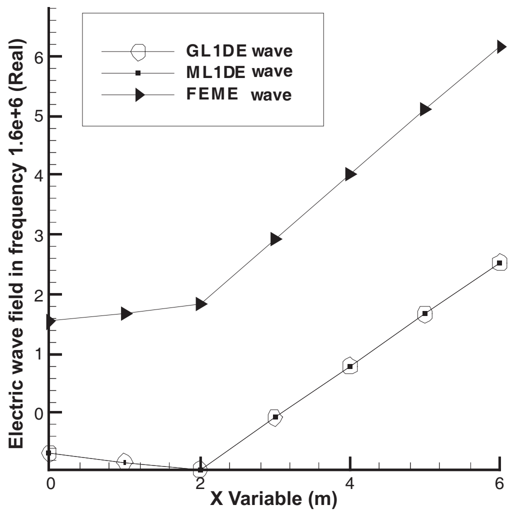

Figure 3: GL, ML and FEM Electric wave with freq. $1.6e^6$ Hz

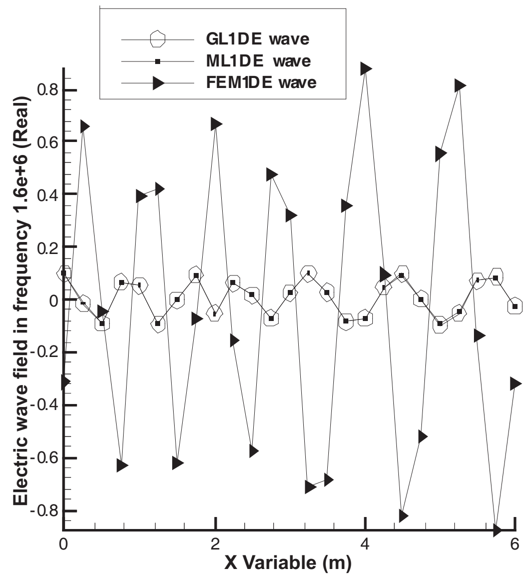

Figure 4: GL, ML and FEM Electric wave with freq. $1.6e^8$ Hz

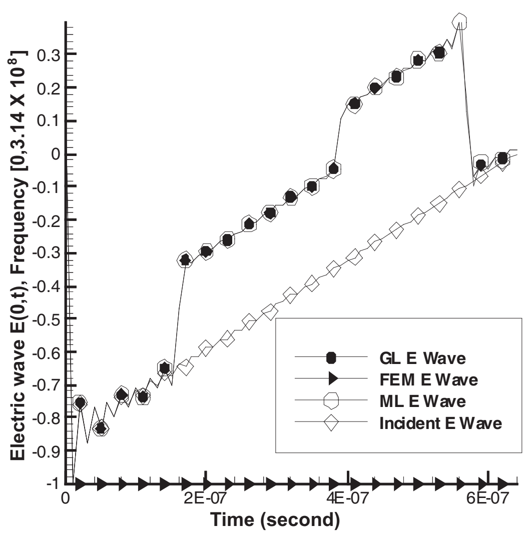

Figure 5: GL, ML and FEM Electric wave E(0,t) in time domain

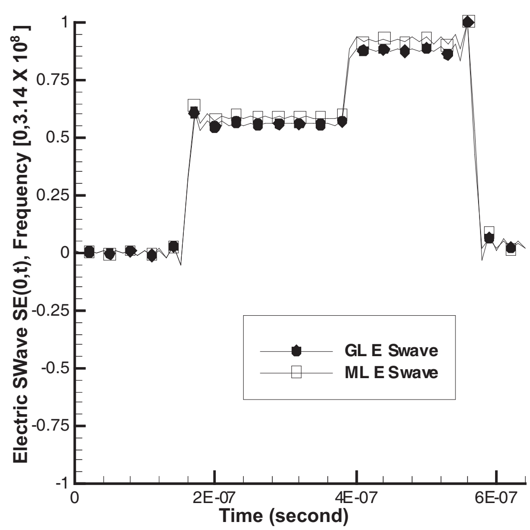

Figure 6: GL and ML Scat. Electric Swave SE(0,t) on time

8. GL Software and Applications and Conclusions

We develope many 3D and 2.5D GL EM, seismic, acoustic, flow, QEM modeling software and some GL EM and seismic inversion software. These GL EM softwares are useful for geophysical EM and seismic exploration; Earthquake EM and seismic exploration; Forest EM and seismic exploration; Environment; EM field in nanometer materials and superconductivity [6]; nondestructive testing imaging [5]; Airborne EM exploration; The stress and displacement analysis in dam, rock, underground structure; the EM Stirring and flow for caster [7]; GPR, radar, and weather imaging; Naiver Stocks weather simulation, etc.. Many applications show that the GL modeling is very fast, low cost and accurate. The GL inversion is stable and high resolution. The GL EM field is fast convergent to exact EM field for high frequency and contrast, while FEM method fails to simulate wave field in the high frequency. The GL method is breakthrough novel method and resolve historical difficulties. GL Geophysical Laboratory and authors have reserved all copyright and patents of 3D/2.5D/2D GL EM, seismic, flow, acoustic QEM modeling and inversion algorithms and have reserved all copyright and patents of the GL software.

REFERENCES

1. Xie, G., J. Li, and F. Xie, "New global and local electromagnetic field (GL) modeling and inversion," *Proceeding of PIERS2005 in Hangzhou*, 68, 2005.
2. Xie, G., F. Xie, and J. Li, "GL EM modeling and inversion based on the new EM integral equation," Report of GLGEO, GLP05001, GLGEO has copyright and patent for the GL method, 2005.
3. Xie, G., J. Li, and F. Xie, "New global and local electromagnetic field modeling and inversion," GLGEO Report GLP04008, GLGEO Copyright, 2004.
4. Xie, G., F. Xie, and J. Li, "New GL and GILD superconductor electromagnetic modeling," *Proceeding of PIERS2005 in Hangzhou*, 187, 2005.
5. Wang, T. and G. Xie, "Nondestructive testing using a new GL electromagnetic inversion," *Proceeding of PIERS2005 in Hangzhou*, 185, 2005.
6. Chang, K. and J. Li, "A laser gauge blocks using GL electromagnetic filed," *Proceeding of PIERS2005 in Hangzhou*, 70, 2005.
7. Li, J., G. Xie, and Z. Liao, "Electromagnetic stirring using GL electromagnetic field," *Proceeding of PIERS2005 in Hangzhou*, 180, 2005.
8. Xie, G., F. Xie, and J. Li, "A new EM integrodierential equation and GL method," *Proceeding of PIERS2005 in Hangzhou*, 294, 2005.
9. Xie, G., J. Li, and F. Xie, "A new GL EM modeling and inversion based on dual boundary integral equation," *Proceeding of PIERS2005 in Hangzhou*, 298, 2005.
10. Xie, G., and J. Li, "A new algorithm for 3-D nonlinear electromagnetic inversion," *3-D Electromagnetic Methods*, SEG book, Editor: Oristaglio and Spies. 193-207, 1999.
11. Xie, G., and J. Li, "New 3D parallel GILD modeling and nonlinear inversion," *IMACS series book in computational and applied math*, Vol. 4, 135-140, 1998.
12. Xie, G., and J. Li, "New parallel SGILD modeling and inversion," *Physics D*, SCI, Vol. 133, 477-487, 1999.
13. Xie, G., J. Li, E. Majer, D. Zuo, and M. Oristaglio, "3-D electromagnetic modeling and nonlinear inversion," *Geophysics*, Vol. 65, No. 3, 804-822, 2000.

Optical Distance and Optical Distance Difference in Moving Systems

G. Korom
Faraday Institute for Theoretical Physics, Hungary

It is shown based on a gedanken-experiment, that the difference of the two wave-propagations and the "optical" path difference (OPD), or more simply the optical distance (OD) is the same only in systems resting in the conductive medium. In case of moving sources and moving observers, the OD is equal with the actual distance of the source and the observer from each other in the phase-space, and is not necessarily equal with the length of the wave propagation across the medium. It has turned out that the phase difference of the amplitude-splitted, and later reunited electromagnetic vibrations in the Michelson-Morley experiment will not change while the speed difference of the Ether-wind is changing, and/or the Michelson Interferometer is rotating. Only phase shifts with equal magnitude will occur at the observers, but the interferometer is insensitive to these shifts, and the observed frequency remains constant because of a double Doppler effect. Consequently, the circular interference fringes observed on the screen will not be dislocated. These results urge the revision of the significance of the Theories operating with relativity of Time and absolute constant light speed, refusing the existence of the Ether. Besides the widely used, derived terminology of "*Optical Path Difference*", author suggests to use — as for the future — the equivalent, directly measurable "*Optical Distance*", and finally, also the "*Optical Distance Difference*" because it describes much better the real physical events going on in the Michelson-Morley experiment.

An Incremental Inductance Approach to Proximity Effect Calculations of Differential Striplines

S. Asgari and M. Tsuk
Ansoft Corporation, USA

The performance of the high-speed digital integrated circuits depends on how well the signal waveforms are controlled on the coupled interconnecting transmission lines whether on-chip or off-chip. Hence, to preserve the signal integrity of the transmitted waveforms traveling with high speed through interconnecting lines requires the designer to analyze a broad band of frequencies.

Meanwhile in many applications, for example the printed circuit board (PCB) layout designs, the differential traces are pushed close to one another. This is done so as to save board space. As a result, the differential impedance will go down for closely spaced lines. Also, the effect of tight coupling decreases the effective trace width causing skin effect loss. This will result in intense concentration of magnetic flux near the corners of the traces, inducing substantial peaking of the current density at the corners. The proximity effect illustrates itself as the concentration of current around the periphery of the signal conductors and the reference planes. The proximity effect increases especially at the very high frequencies.

While usually different 2D and 3D field solvers such as Ansoft's SI2d and HFSS are used to do a more elaborate surface resistance calculation, no closed form equations that we know of are available to do an adequate approximation of the proximity effect even for the simpler case of symmetric differential striplines. In this paper, we derive closed form equations for the effective surface resistance matrix of symmetric edge-coupled differential stripline based on Wheeler's incremental inductance rule while incorporating the proximity effects of the lines. This methodology can be generalized to non-symmetric as well as multi-coupled lines.

The paper is organized as follows. In section II, we review Wheeler's incremental inductance rule and set up the general formulas needed to solve for the resistance matrix. In section III, we present the closed form equations for the resistance matrix and summarize the equations for the case of differential stripline. In section IV, we show few examples and simulation results which demonstrate the usefulness of our approach as compared to that of Ansoft's SI2d as well as Moments method (MOM) calculations. Finally we end the paper with concluding remarks and future extension of the work.

MATLAB SIMULINK Based DQ Modeling and Dynamic Characteristics of Three Phase Self Excited Induction Generator

A. Kishore, R. C. Prasad, and B. M. Karan
Birla Institute of Technology, India

Abstract—In this paper, DQ-modeling approach for Transient State analysis in the time domain of the three-phase self-excited induction generator (SEIG) with squirrel cage rotor is presented along with its operating performance evaluations. The three-phase SEIG is driven by a variable-speed prime mover (VSPM) such as a wind turbine for the clean alternative renewable energy in rural areas. Here the prime mover speed has been taken both as fixed and variable and results have been analyzed. The basic Dynamic characteristics of the VSPM are considered in the three-phase SEIG approximate electrical equivalent circuit and the operating performances of the three-phase SEIG coupled by a VSPM in the Transient state analysis are evaluated and discussed on the conditions related to transient occurs in the system and speed changes of the prime mover.

The whole proposed system has been developed and designed using MATLAB / SIMULINK.

1. Introduction

A wind electrical generation system is the most cost competitive of all the environmentally clean and safe renewable energy sources in the world. It is well known that the three phase self excited induction machine can be made to work as a self-excited induction generator [3, 4], provided capacitance should have sufficient charge to provide necessary initial magnetizing current[5, 6]. In an externally driven three phase induction motor, if a three phase capacitor bank is connected across it's stator terminals, an EMF is induced in the machine windings due to the self excitation provided by the capacitors. The magnetizing requirement of the machine is supplied by the capacitors. For self excitation to occur, the following two conditions must be satisfied:

1 The rotor should have sufficient residual magnetism.

2 The three capacitor bank should be of sufficient value.

If an appropriate capacitor bank is connected across the terminals of an externally driven Induction machine and if the rotor has sufficient residual magnetism an EMF is induced in the machine windings due to the excitation provided by the capacitor. The EMF if sufficient would circulate leading currents in the capacitors. The flux produced due to these currents would assist the residual magnetism. This would increase the machine flux and larger EMF will be induced. This in turn increases the currents and the flux. The induced voltage and the current will continue to rise until the VAR supplied by the capacitor is balanced by the VAR demanded by the machine, a condition which is essentially decided by the saturation of the magnetic circuit. This process is thus cumulative and the induced voltage keeps on rising until saturation is reached. To start with transient analysis the dynamic modeling of induction motor has been used which further converted into induction generator [8, 11]. Magnetizing inductance is the main factor for voltage buildup and stabilization of generated voltage for unloaded and loaded conditions. The dynamic Model of Self Excited Induction Generator is helpful to analyze all characteristic especially dynamic characteristics. To develop dynamic model of SEIG we first develop the dynamic model of three phase induction motor in which the three phase to two phase conversion has been done using Park's transformation, then all the equations have been developed. The traditional tests used to determine the parameters for the equivalent circuit model are open circuit and short circuit test. In this paper the DQ model shown in Fig. 1 has been used to obtain the dynamic characteristics and further a flux oriented controller is proposed to improve the dynamic characteristics.

2. Modeling of Self Excited Induction Generator

The equation shown is used for developing the dynamic model of SEIG

$$[V_G] = [R_G][i_G] + [L_G]p[i_G] + w_{rG}[G_G][i_G] \tag{1}$$

Where **p** represents the derivative w. r. t. time, $[V_G]$ and $[i_G]$ represents 4×1 column matrices of voltage and which is given as $[V_G] = [V_{sd} \quad V_{sq} \quad V_{rd} \quad V_{rq}]^T$ and $[I_G] = [i_{sd} \quad i_{sq} \quad i_{rd} \quad i_{rq}]^T$ $[R]$, $[L]$ and $[G]$ represents 4×4

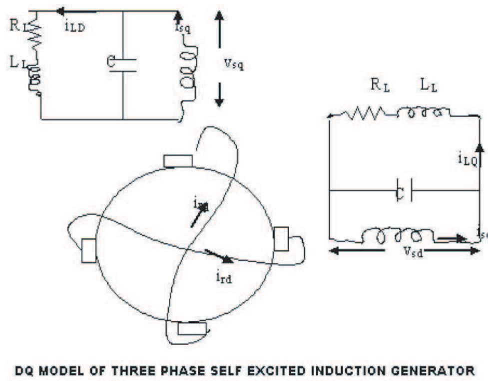

Figure 1: DQ model of three phase induction generator.

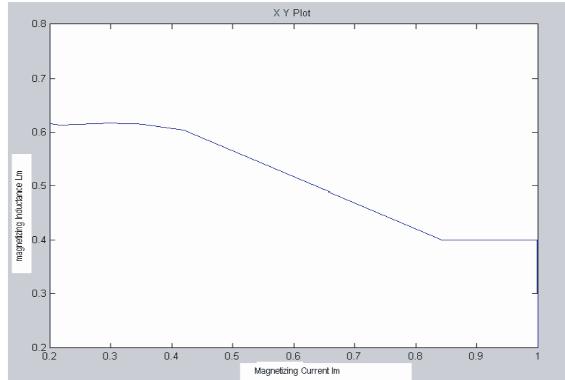

Figure 2: Magnetizing inductance Vs magnetizing current.

matrices of resistance, generator inductance and conductance as given. Further Lm the magnetizing inductance, which can be obtained from the magnetizing curve of the machine shown in Fig. 2,

$$[L] = \begin{bmatrix} L_{sd} & L_{dq} & L_{md} & L_{dq} \\ L_{dq} & L_{sq} & L_{dq} & L_{md} \\ L_{md} & L_{dq} & L_{rd} & L_{dq} \\ L_{dq} & L_{mq} & L_{dq} & L_{rq} \end{bmatrix} [G] = \begin{bmatrix} 0 & 0 & 0 & 0 \\ 0 & 0 & 0 & 0 \\ 0 & L_m & 0 & L_r \\ -L_m & 0 & -L_r & 0 \end{bmatrix} [L] = \begin{bmatrix} L_s & 0 & L_m & 0 \\ 0 & L_s & 0 & L_m \\ L_m & 0 & L_r & 0 \\ 0 & L_m & 0 & L_r \end{bmatrix}$$

The Relation between L_m and i_m is given as

$$L_m = |\Psi_m|/|i_m| \tag{2}$$

Where $|\Psi_m|$ and i_m are the magnetizing flux linkage and magnetizing current. The equation defining L_m Vs $|i_m|$ used in the model is

$$|i_m| = 1.447 * L_m^6 - 8.534 * L_m^5 + 18.174 * L_m^4 - 17.443 * L_m^3 + 7.322 * L_m^2 - 1.329 * L_m + 0.6979 \tag{3}$$

L_{dq} used in matrix L represent the cross saturation coupling between all axes in space quadrature and is due to saturation. $L_{dq} = L_m + i_{md}/i_{mq} * L_{dq}$, $L_{mq} = L_m + i_{mq}/i_{mq} * L_{dq}$. It follows that above equations representing L_{dq}, L_{md}, and L_{mq} that under linear magnetic conditions, $L_{dq} = 0$ and $L_{md} = L_{mq} = L_m$, as expected. The two axes values of the total stator and rotor inductances are $L_{sd} = L_{s1} + L_{md}$, $L_{sq} = L_{s1} + L_{mq}$ and $L_{rd} = L_{r1} + L_{md}$, $L_{rq} = L_{r1} + L_{mq}$.

The above equations L_{s1} and L_{r1} are the leakage inductances of the stator and rotor, respectively. Because of saturation, L_{sd} ? L_{sq}, but it follows from previous arguments that under linear magnetic conditions $L_{sd} = L_{sq}$. Hence $L_r = L_{r1} + L_m$

The electromagnetic torque developed by the generator is given by

$$T_e = (3/4) * P * L_m * (i_{sq} \quad i_{rd} - i_{sd} \quad i_{rq}) \tag{4}$$

Thus it sees that Eq. (1) consists of four first order equations. An induction motor is hence represented by these four first order differential equations. Because of the non-linear nature of the magnetic circuit, the magnitude of magnetizing current, I_m is calculated as

$$I_m = [(i_{sd} + i_{rd})^2 + (i_{sq} + i_{rq})^2]^{1/2} \tag{5}$$

Capacitor side equations are

$$p[v_{sG}] = (1/C)[i_C] \tag{6}$$

further

$$[i_C] = [i_{sG}] + [i_L] \tag{7}$$

Where $[v_{sG}]$, $[i_{sG}]$, $[i_L]$ Column matrices representing direct and quadrature axis component of capacitor current generator stator current and load current respectively.

Load Side Equations

$$[v_{sG}] = L_L\, p\, [i_L] + R_L[i_L] \tag{8}$$

Thus it is seen that complete transient model of the SEIG in d-q axis quasi stationary reference frame consists of equations from (1) to (8).

3. Modeling of Self Excited Induction Generator Using MATLAB SIMULINK

MATAB SIMULINK is powerful software tool for modeling and simulation and accepted globally. The equations from (1) to (8) have been implemented in MATLAB SIMULINK using different blocks. In this paper the step by step modeling of SEIG using SIMULINK has been described.

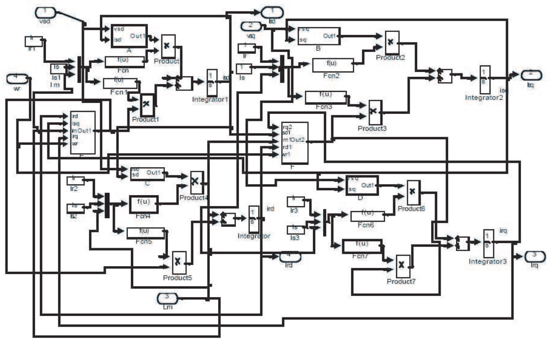

Figure 3: Stator and rotor dq currents.

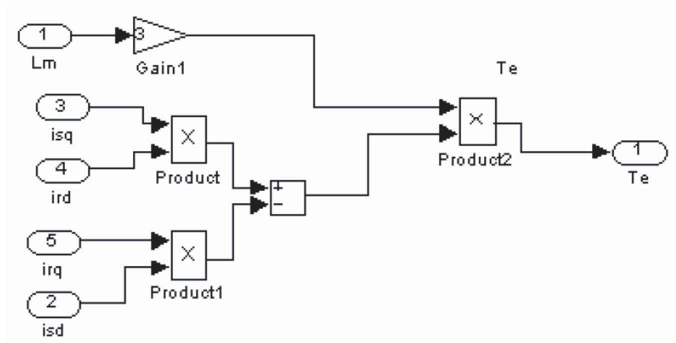

Figure 4: Electromagnetic torque generated.

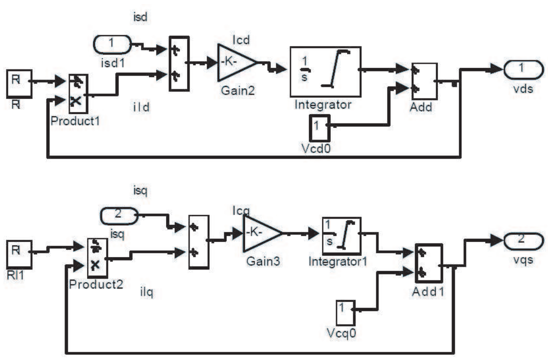

Figure 5: Load voltages.

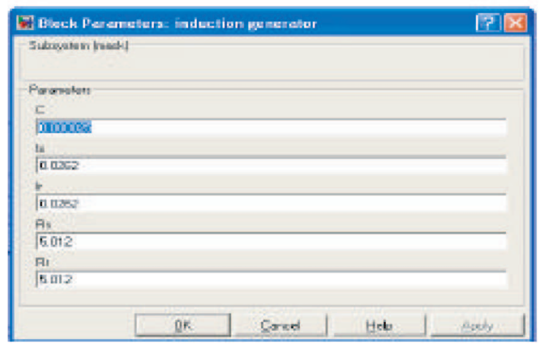

Figure 6: SEIG parameters.

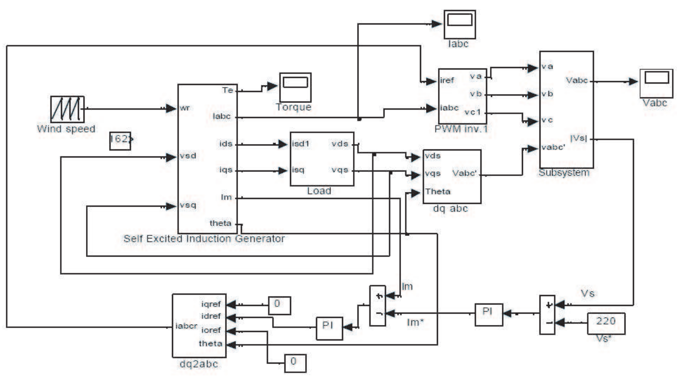

Figure 7: Simulink model of proposed system.

Equation (1) shown has four first order differential equations, for which the solutions gives the four currents (stator d-q axis currents and rotor d-q axis currents). Further these currents are the function of constants viz. Stator and rotor Inductances and Resistances, speed, Excitation Capacitance, load resistances. And also variables like Magnetizing Inductance, Magnetizing currents, Electromagnetic torque generated, has been evaluated using (3) to (5). The constraints of non linear magnetizing inductance have been taken into accounts, the curve between Non linear magnetizing inductance vs magnetizing currents is shown in Fig. 2. The equation of this non linear graph has been obtained by curve fitting and hence sixth order nonlinear polynomial equation which is showing the relation between magnetizing inductance vs Magnetizing current. This equation has been implemented using function block in SIMULINK block sets. In Fig. 3, the SIMULINK model of stator and rotor dq currents has been shown, Similarly Fig. 4, shows the electromagnetic torque generated. The load block in which the stator voltage determined has been shown in Fig. 5. To put the various parameters the masking of overall blocks has been done. The values and the masked blocks have been shown in Fig. 6.

4. Modeling Using MATLAB SIMULINK

The equation above described has been implemented in MATLAB / SIMULINK block sets. The equations from 1 to 7 have been implemented in subsystem "Self Excited Induction Generator" whose outputs are Torque, currents, rotor angle (theta), magnetizing current. Similarly the other blocks are Inverter, load, and a subsystem to find three phase voltages.

5. Results and Discussions

The Model has been simulated using MATLAB/SIMULINK shown in Fig. 7. The analysis has been done taking various constraints mainly-(i) assuming constant speed and no controller (Fig. 8), (ii) assuming variable speed without controller (Fig. 9), (iii) Constant speed which going to constant at 0.1 sec with controller (Fig. 10). And finally (iv) variable speed with controller (Fig. 11).

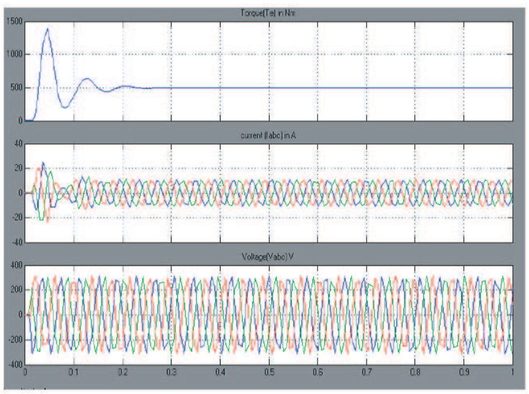

Figure 8: Electromagnetic torque, three phase voltage, current at constant wind speed.

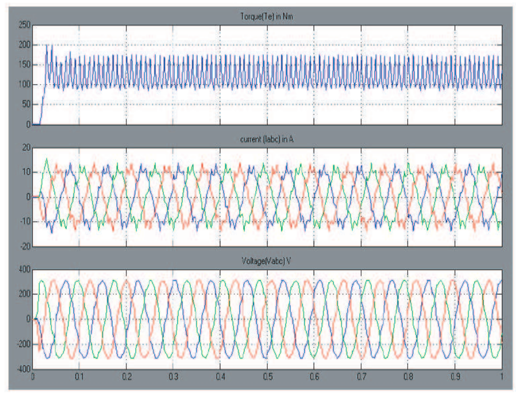

Figure 9: Electromagnetic torques, three phase voltage, current at variable wind speed without controller.

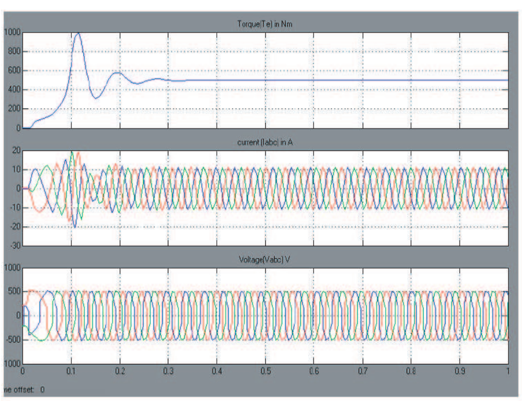

Figure 10: Electromagnetic torque, three phase voltage, current at constant wind speed with controller.

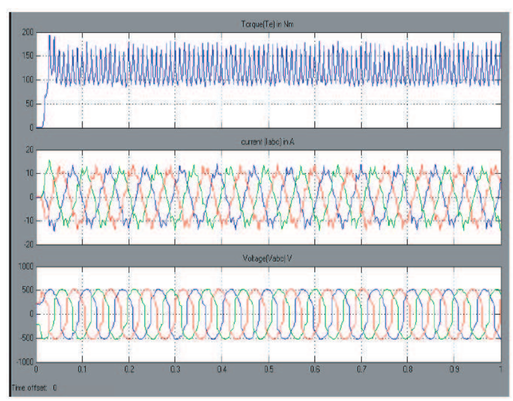

Figure 11: Electromagnetic torque, three phase voltage, current at variable wind speed with controller.

In first case the electromagnetic torque generated has been reached to steady state 0.2 second. Initially transients occur at 0.05 sec when currents goes to 10 ampere provided constant voltage. Note that load is constant all the time and for sake of simplicity resistive load has been considered. In second case the variable wind speed has been considered. To implement the variable speed in SIMULINK a repeating sequence block has been used. It has been observed that the electromagnetic torque developed has been a vibrations in steady state. The currents in this case have some ripple in the waveform. In the third case the controller has been implemented and response has been observed. A ramp signal has been taken which further becomes constant at 0.05 sec, as constant speed starting from zero. As a result a transient has been occurring at 0.05 sec which then comes to steady state at 0.1 sec. And finally the wind speed has been taken as variable speed with controller has been implemented which result no transients has been occur at output currents but some ripples have been still remaining in currents waveform as shown in Fig. 9.

6. Conclusions

Self Excited Induction generator has been found suitable applicability for isolate applications. The estimation of non linear magnetizing inductance is the main factor of converting the Induction motor as self excitation induction generator. To develop the system as wider applicability the controller has been designed to improve the dynamic characteristics of the system. It has been shown that the transients have been removed when controller has been implemented.

7. Specifications of the Machine

10 h.p (7.5 kW), 3-phase, 4 poles, 50 Hz, 415 volts, 3.8 A Delta connection,
Base Voltage / Rated Voltage = 415 V
Base Current / Rated Current = 2.2 A
Rs = 1.0 ohm
Rr = 0.77 ohm
Xls = Xlr = 1.0 ohm
J = 0.1384 kg-m^2

REFERENCES

1. John, G., W. Erdman, R. Husdon, C. S. Fan, and S. Mahajan, "Stator flux estimation from inverter states for the field oriented control of induction generators," *IEEE*, 1995.
2. Farret, F. A., B. Palle, and M. G. Simoes, "A full expandable model of parallel self excited induction generators," 2005.
3. Daher, S., R. Pontes, and F. Auntunes, "A stand alone three phase induction generator based wind energy storage system," *IEEE*, 1999.
4. Chaturvedi, R. and S. S. Murthy, "Use of conventional induction motor as a wind driven self excited induction generator for autonomous operation," *IEEE*, 1998.
5. Harrington, R. J. and F. M. M. Bassiouny, "New approach to determine the critical capacitance for self excited induction generators," *IEEE Transaction on Energy Conversion*, Vol. 13, No. 3, September 1998.
6. Sridhar, L., B. Singh, and C. S. Jha, "A steps towards improvements in the characteristics of a self excited induction generators," *IEEE Transaction on Energy Conversion*, Vol. 8, No. 1, March 1993.
7. Singh, S. P., B. Singh, and M. P. Jain, "Comparative study on the performance of commercially designed induction generator with induction motors operating as self excited induction generators," *IEE Proceedings-C*, Vol. 140, September 1993.
8. Sridhar, L., B. Singh, C. S. Jha, and B. P. Singh, "Analysis of a self excited induction generator feeding induction motor load," *IEEE Transaction on Energy Conversion*, Vol. 9, No. 2, June 1994.
9. Sridhar, L., B. Singh, and C. S. Jha, "Improvements in the performance of a self excited induction generator through series compensation," *IEE Proc.-Gener. Trans. Distrib.*, Vol. 146, No. 6. November 1999.3
10. Singh, S. P., B. Singh, and M. P. Jain, "Performance characteristics and optimum utilization of a cage machine as a capacitor excited induction generator," *IEEE Transaction on Energy Conversion*, Vol. 5, No. 4, December 1990.
11. Singh, S. P., B. Singh, and M. P. Jain, "Performance characteristics and optimum utilization of a cage machine as a capacitor excited induction generator," *IEEE Transaction on Energy Conversion*, Vol. 5, No. 4, December 1990.
12. Sridhar, L., B. Singh, and C. S. Jha, "Transient performance of the self regulated short shunt self excited induction generator," *IEEE Transaction on Energy Conversion*, Vol. 10, No. 2, June 1995.

Estimation of Higher Order Correlation between Electromagnetic and Sound Waves Leaked from VDT Environment Based on Fuzzy Probability and the Prediction of Probability Distribution

A. Ikuta, **M. Ohta**, and **H. Ogawa**
Prefectural University of Hiroshima, Japan

Abstract—In this paper, a signal processing method considering not only linear correlation but also the higher order nonlinear correlation information is proposed on the basis of fuzzy observation data, in order to find the mutual relationship between sound and electromagnetic waves leaked from electronic information equipment. More specifically, by applying the well-known fuzzy probability to an expression on the multi-dimensional probability distribution in an orthogonal expansion series form reflecting systematically various types of correlation information, a method to estimate precisely the correlation information between the variables from the conditional moment statistics of fuzzy variables is proposed. The effectiveness of the proposed theory is experimentally confirmed by applying it to the observation data leaked from VDT in the actual work environment.

1. Introduction

Some studies on the mutual relationship between sound and electromagnetic waves leaked from electronic equipment in the actual working environment have become important recently because of the increased use of various information and communication systems like the personal computer and portable radio transmitters [1, 2], especially concerning their individual and/or compound effects on a living body. Sound and electromagnetic waves, especially, are often measured in a frequency domain under the standardized measuring situation in a reverberation room, anechoic room and radiofrequency anechoic chamber. Though these standard methods in a frequency domain are useful for the purpose of analyzing the mechanism of individual phenomena, they seem to be inadequate for evaluating total effects on the compound or the mutual relationship between sound and electromagnetic waves in complicated circumstances, such as the actual working environment. In order to evaluate universally the mutual correlation characteristics and its total image in the actual complex working environment, it is necessary to introduce some signal processing methods, especially in a time domain.

On the other hand, the actual observed data often contain fuzziness due to confidence limitations in sensing devices, permissible errors in the experimental data, and quantizing errors in digital observations. Therefore, in order to evaluate precisely the objective sound and electromagnetic environments, it is desirable to estimate the mutual relationship between sound and electromagnetic waves based on the fuzzy observations.

In this study, a signal processing method considering not only linear correlation but also the higher order nonlinear correlation information is proposed on the basis of fuzzy observation data, in order to find the mutual relationship between sound and electromagnetic waves leaked from electronic information equipment. More specifically, a conditional probability expression for fuzzy variables is first derived by applying the fuzzy probability [3] to a multi-dimensional joint probability function in a series type expression reflecting information on various correlation relationships between the variables. Next, by use of the derived probability expression, a method for estimating precisely the correlation information from various conditional moment statistics based on the observed fuzzy data is theoretically proposed. On the basis of the estimated correlation information, the probability distribution for a specific variable (e. g., electromagnetic wave) based on the observed fuzzy data of the other variable (e. g., sound) can be predicted. Finally by applying the proposed methodology to the measurement fuzzy data in an actual working environment, the effectiveness of theory is confirmed experimentally.

2. Prediction of Specific Probability Distribution from Arbitrary Fuzzy Fluctuation Factor

The observed data in the actual sound and electromagnetic environments often contain fuzziness due to several factors such as limitations in the measuring instruments, permissible error tolerances in the measurement, and quantization errors in digitizing the observed data.

In order to evaluate quantitatively the complicated relationship between sound and electromagnetic waves leaked from an identical electronic information equipment, let two kinds of variables (i. e., sound and electromagnetic waves) be x and y, and the observed data based on fuzzy observations be X and Y respectively. There exist the mutual relationships between x and y, and also between X and Y. Therefore, by finding the relations between x and X, and also between y and Y, based on the fuzzy probability [3], it is possible to predict the true value y (or x) from the observed fuzzy data X (or Y). For example, for the prediction of the pdf (probability density function) $P_s(y)$ of y from X, averaging the conditional pdf $P(y|X)$ on the basis of the observed fuzzy data X, $P_s(y)$ can be obtained as: $P_s(y) =< P(y|X) >_X$. The conditional pdf $P(y|X)$ can be expressed under the employment of the well-known Bayes' theorem:

$$P(y|X) = \frac{P(X,y)}{P(X)}. \tag{1}$$

The joint probability distribution $P(X,y)$ is expanded into an orthonormal polynomial series on the basis of the fundamental probability distribution $P_0(X)$ and $P_0(y)$, which can be artificially chosen as the probability function describing approximately the dominant parts of the actual fluctuation pattern, as follows:

$$\begin{aligned} P(X,y) &= P_0(X)P_0(y)\sum_{m=0}^{\infty}\sum_{n=0}^{\infty} A_{mn}\psi_m(X)\phi_n(y), \\ A_{mn} &= <\psi_m(X)\phi_n(y)>. \end{aligned} \tag{2}$$

The information on the various types of linear and nonlinear correlations between X and y is reflected in each expansion coefficient A_{MN}. When X is a fuzzy number expressing an approximated value, it can be treated as a discrete variable with a certain level difference. Therefore, as the fundamental probability function $P_0(X)$, the generalized binomial distribution with a level difference interval h_X can be chosen:

$$\begin{aligned} P_0(X) &= \frac{(\frac{N_X-M_X}{h_X})!}{(\frac{X-M_X}{h_X})!(\frac{N_X-X}{h_X})!} p_X^{\frac{X-M_X}{h_X}}(1-p_X)^{\frac{N_X-X}{h_X}}, \\ p_X &= \frac{\mu_X - M_X}{N_X - M_X},\ \mu_X =< X >, \end{aligned} \tag{3}$$

where M_X and N_X are the maximum and minimum values of X. Furthermore, as the fundamental pdf $P_0(y)$ of y, the standard Gaussian distribution is adopted:

$$\begin{aligned} P_0(y) &= \frac{1}{\sqrt{2\pi\sigma_y^2}} exp\{-\frac{(y-\mu)^2}{2\sigma_y^2}\}, \\ \mu_y &= < y >,\ \sigma_y^2 =< (y-\mu_y)^2 >. \end{aligned} \tag{4}$$

The orthonormal polynomials $\psi_m(X)$ and $\phi_n(y)$ with the weighting functions $P_0(X)$ and $P_0(y)$ can be determined as [4]

$$\begin{aligned} \psi_m(X) &= \{(\frac{N_X-M_X}{h_X})^{(m)} m!\}^{-\frac{1}{2}} (\frac{1-p_X}{p_X})^{\frac{m}{2}} \frac{1}{h_X^m} \\ &\cdot \sum_{j=0}^{m} \frac{m!}{(m-j)!j!}(-1)^{m-j}(\frac{p_X}{1-p_X})^{m-j}(N_X-X)^{(m-j)}(X-M_X)^{(j)}, \\ (X^{(n)} &= X(X-h_X)\cdots(X-(n-1)h_X),\ X^{(0)}=1), \end{aligned} \tag{5}$$

$$\phi_n(y) = \frac{1}{\sqrt{n!}} H_n(\frac{y-\mu_y}{\sigma_y});\ Hermite\ polynomial \tag{6}$$

Thus, the predicted pdf $P_s(y)$ can be expressed in an expansion series form:

$$P_s(y) = P_0(y)\sum_{n=0}^{\infty} < \frac{\sum_{m=0}^{\infty} A_{mn}\psi_m(X)}{\sum_{n=0}^{\infty} A_{m0}\psi_m(X)} >_X \phi_n(y). \tag{7}$$

3. Estimation of Correlation Information Based on Fuzzy Observation Data

The expansion coefficient A_{mn} in (2) has to be estimated on the basis of the fuzzy observation data X and Y, when the true value y is unknown. Let the joint probability distribution of X and Y be $P(X,Y)$, and the joint pdf of x and y be $P(x,y)$. By applying fuzzy probability [3] to $P(X,y)$, $P(X,Y)$ can be expressed as:

$$P(X,Y) = \frac{1}{K}\int \mu_Y(y)P(X,y)dy, \qquad (8)$$
$$(K \quad : \quad a\ constant\ satisfying\ the\ normalized\ condition: \sum_X \sum_Y P(X,Y) = 1).$$

The fuzziness of Y can be characterized by the membership function $\mu_Y(y)(= exp\{-\alpha(y-Y)^2\}$, α; a parameter).

Substituting (2) in (8), the following relationship is derived.

$$P(X,Y) = \frac{1}{K}P_0(X)\sum_{m=0}^{\infty}\sum_{n=0}^{\infty}A_{mn}a_n\psi_m(X),$$
$$a_n = \int exp\{-\alpha(y-Y)^2\}P_0(y)\psi_n(y)dy. \qquad (9)$$

The conditional Nth order moment of the fuzzy variable X is given from (9) as

$$< X^N|Y > = \sum_X X^N P(X|Y) = \sum_X X^N P(X,Y)/P(Y)$$
$$= \sum_X X^N P_0(X)\sum_{m=0}^{\infty}\sum_{n=0}^{\infty}A_{mn}a_n\psi_m(X)/\sum_{n=0}^{\infty}A_{0n}a_n. \qquad (10)$$

After expanding X^N in an orthogonal series expression, by considering the orthonormal relationship of $\psi_m(X)$. (10) is expressed explicitly as

$$< X^N|Y >= \sum_{m=0}^{\infty}\sum_{n=0}^{\infty}d_m^N A_{mn}a_n/\sum_{n=0}^{\infty}A_{0n}a_n,$$
$$(X^N = \sum_{m=0}^{N}d_m^N\psi_m(X),\ d_m^N;\ appropriate\ constant). \qquad (11)$$

The right side of the above equation can be evaluated numerically from the fuzzy observation data. Accordingly, by regarding the expansion coefficients A_{mn} as unknown parameters, a set of simultaneous equations in the same form as in (11) can be obtained by selecting a set of N and/or Y values equal to the number of unknown parameters. By solving the simultaneous equations, the expansion coefficients A_{mn} can be estimated. Furthermore, using these estimates, the pdf $P_s(y)$ can be predicted from (7).

4. Mutual Relationship between Sound and Electric Field from a VDT in Actual Working Environment

By adopting a personal computer in the actual working environment as specific information equipment, the proposed method is applied to investigate the mutual relationship between sound and electromagnetic waves leaked from a VDT under the situation of playing a computer game. In order to eliminate the effects of sound from outside, a personal computer is located in an anechoic room (cf. Fig. 1). The RMS value (V/m) of the electric field radiated from the VDT and the sound intensity level (dB) emitted from a speaker of the personal computer are simultaneously measured. The data of electric field strength and sound intensity level are measured by use of a electromagnetic field survey mater and a sound level meter respectively. The slowly changing nonstationary 600 data for each variable are sampled with a sampling interval of 1 [s]. Two kinds of fuzzy data with the quantized level widths of 0.1 [v/m] for electric field strength and 5.0 [dB] for sound intensity level are obtained. Based on the 400 data points, the expansion coefficients A_{mn} are first estimated by use of (11). Next, the 200 sampled data within the different time interval which are nonstationally different from data used for the estimation of the expansion coefficients are adopted for predicting the probability distributions of

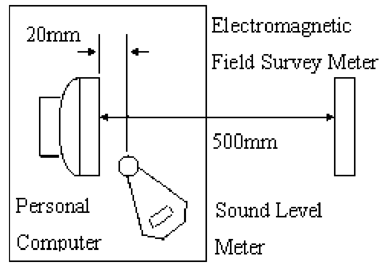

Figure 1: A schematic drawing of the experiment.

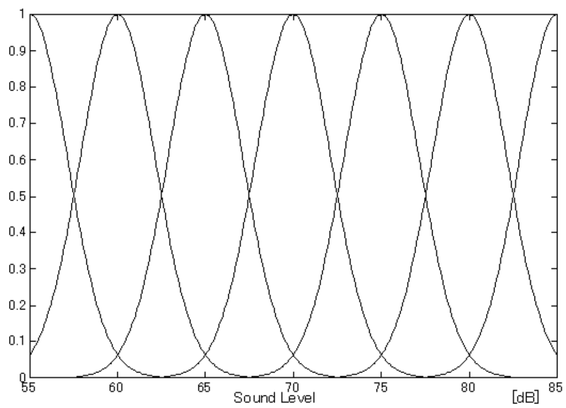

Figure 2: Membership function of sound level.

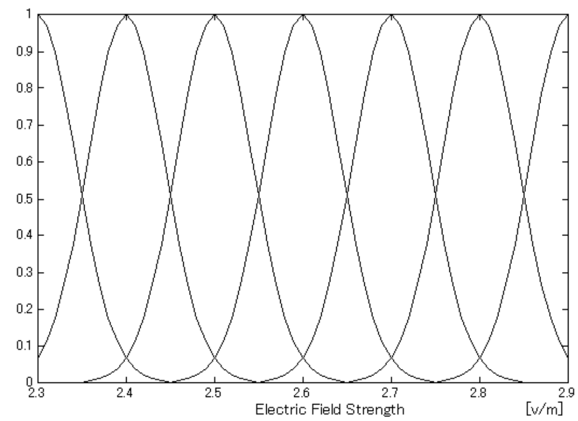

Figure 3: Membership function of electric field.

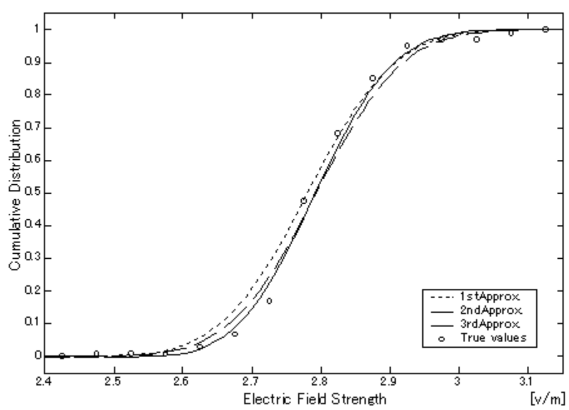

Figure 4: Prediction of the cumulative distribution for the electric field strength based on the fuzzy observation of sound.

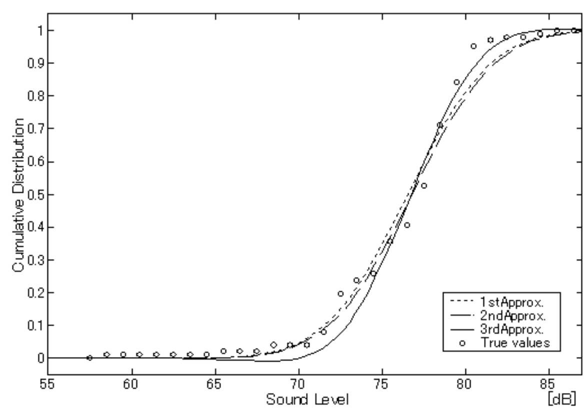

Figure 5: Prediction of the cumulative distribution for the sound level based on the fuzzy observation of electric field.

(i) the electric field based on sound and (ii) the sound based on electric field. Membership functions of the sound level and electric field are shown in Figs. 2 and 3. The parameter α is decided so as to express the distribution of data as precisely as possible.

The experimental results for the prediction of electric field strength and sound level are shown in Figs. 4 and 5 respectively in a form of cumulative distribution. From these figures, it can be found that the theoretically predicted curves show good agreements with experimental sample points by considering the expansion coefficients with several higher orders.

For comparison, the generalized regression analysis method [4] previously reported is applied to fuzzy observation data as a trial. After paying our attention to the probability distribution without considering any membership function, the probability distribution Y can be predicted on the basis of fuzzy observation daya X. The predicted results for electric field strength and sound level are shown in Figs. 6 and 7 respectively.

The theoretical curves show large prediction error to the true values as compared with the prediction results in Figs. 4 and 5. These results clearly show the effectiveness of the proposed method for application to the fuzzy observation data.

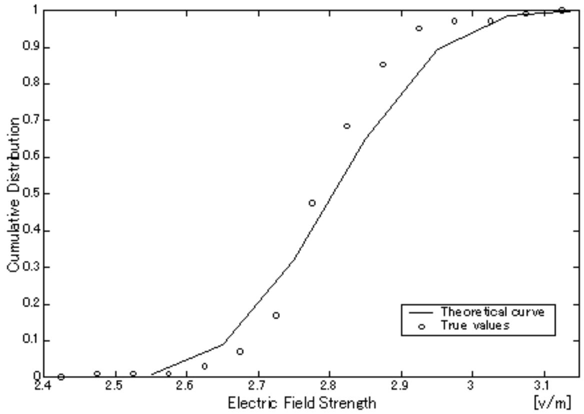

Figure 6: Prediction of the cumulative distribution for the electric field strength by use of the extended regression analysis method.

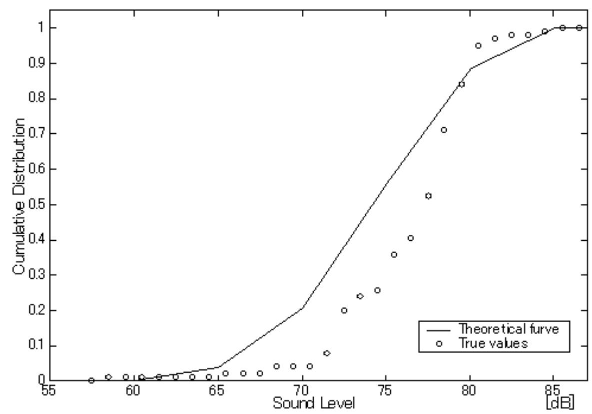

Figure 7: Prediction of the cumulative distribution for the sound level by use of the extended regression analysis method.

5. Conclusion

In this paper, a signal processing method has been proposed in order to grasp minutely and universally the mutual relationship between sound and electromagnetic waves leaked from electronic information equipment. More specifically, based on the fuzzy observation data on the sound and electromagnetic waves, a method to estimate not only the linear correlation of lower order but also the nonlinear correlation information of higher order between both variables has been derived by introducing the fuzzy probability. The validity and effectiveness of the proposed method have been confirmed experimentally by applying it to the observation data radiated from a personal computer in an actual working environment playing a computer game.

REFERENCES

1. Ikuta, A., M. Ohta, and H. Ogawa, "Various regression characteristics with higher order among light, sound and electromagnetic waves leaked from VDTMeasurement and signal processing in the actual working environment," *J. of the International Measurement Confederation*, Vol. 21, 25–33, 1997.
2. Ohta, M., and A. Ikuta, "Applicability of two stochastic evaluation methods to electromagnetic waves in near field leaked from ITE group under parallel working situationIntroduction of some composition principle in space and time domain," *Progress In Electromagnetic Research*, Vol. 38, 269–281, 2002.
3. Zadeh, L. A., "Probability measures of fuzzy events," *J. Math. Anal. Appl.*, Vol. 23, 421–427, 1968.
4. Ohta, M., A. Ikuta, and N. Takaki, "A new trial of regression analysis with less information loss and its application to sound insulation wallsMatching to the prediction of response probability distribution," *J. of the Acoustical Society of Japan*, Vol. 44, 848–856, Japanese, 1988.

A Single Phase Single Stage AC/DC Converter with High Input Power Factor and Tight Output Voltage Regulation

A. K. Jha
Birla Instt. of Technology, India

B. G. Fernandes and A. Kishore
Indian Institute of Technology, India

Abstract—A single stage single switch AC/DC converter is an integration of input current shaper and a DC/DC cell with a shared controller and one active switch. The converter is applicable for digital input power supply with high input power factor and tight output voltage regulation. The focus of the topology is to reduce the DC bus voltage at light load without compromising with input power factor and voltage regulation. The concept behind this topology is direct power transfer scheme. Using special configuration of DC/DC cell does reduction of DC bus voltage and DC/DC cell works on the principle of series charging and parallel discharging. The power output of this converter can go up to 200 W.

1. Introduction

An ac to dc converter is an integral part of any power supply unit used in the all electronic equipments. Also, it is used as an interface between utility and most of the power electronic equipments. These electronic equipments form a major part of load on the utility. Generally, to convert line frequency ac to dc, a line frequency diode bridge rectifier is used. To reduce the ripple in the dc output voltage, a large filter capacitor is used at the rectifier output. But due to this large capacitor, the current drawn by this converter is peaky in nature. This input current is rich in low order harmonics. Also, as power electronics equipments are increasingly being used in power conversion, they inject low order harmonics into the utility. Due to the presence of these harmonics, the total harmonic distortion is high and the input power factor is poor. Due to problems associated with low power factor and harmonics, utilities will enforce harmonic standards and guidelines which will limit the amount of current distortion allowed into the utility and thus the simple diode rectifiers may not in use. So, there is a need to achieve rectification at close to unity power factor and low input current distortion. Initially, power factor correction schemes have been implemented mainly for heavy industrial loads like induction motors, induction heating furnaces etc., which forms a major part of lagging power factor load. However, the trend is changing as electronic equipments are increasingly being used in everyday life nowadays. Hence, PFC is becoming an important aspect even for low power application electronic equipments.

The objective of the paper has been in the direction of better understanding of direct power transfer scheme, closed loop simulation and analysis of proposed AC/DC converter. Emphasis of the paper has been the design of 100 W AC/DC converter with high input power factor and tight output voltage regulation without compromising with high DC bus voltage at light loading condition.

2. Power Factor Correction Techniques

In recent years, single-phase switch-mode AC/DC power converters have been increasingly used in the industrial, commercial, residential, aerospace, and military environment due to advantages of high efficiency, smaller size and weight. However, the proliferation of the power converters draw pulsating input current from the utility line, this not only reduce the input power factor of the converters but also injects a significant amount of harmonic current into the utility line [1]. To improve the power quality, various PFC schemes have been proposed. There are harmonic norms such as IEC 1000-3-2 introduced for improving power quality. By the introduction of harmonic norms now power supply manufacturers have to follow these norms strictly for the remedy of signal interference problem [2].

The various methods of power factor correction can be classified as:

(1) Passive power factor correction techniques

(2) Active power factor correction techniques

In passive power factor correction techniques, an LC filter is inserted between the AC mains line and the input port of the diode rectifier of AC/DC converter as shown in Figure 1. This technique is simple and rugged but it has bulky size and heavy weight and the power factor cannot be very high [1]. Therefore it is now not applicable for the current trends of harmonic norms. Basically it is applicable for power rating of lower than 25 W. For higher power rating it will be bulky.

In active power factor correction techniques approach, switched mode power supply (SMPS) technique is used to shape the input current in phase with the input voltage. Thus, the power factor can reach up to unity. Figure 2 shows the circuit diagram of basic active power correction technique [2]. By the introduction of regulation norms IEC 1000-3-2 active power factor correction technique is used now a day. There are different topologies for implementing active power factor correction techniques. Basically in this technique power factor correcting cell is used for tracking the input current in phase of input voltage such that input power factor come up to unity. Comparing with the passive PFC techniques, active PFC techniques have many advantages such as, high power factor, reduced harmonics, smaller size and light-weight. However, the complexity and relatively higher cost are the main drawbacks of this approach.

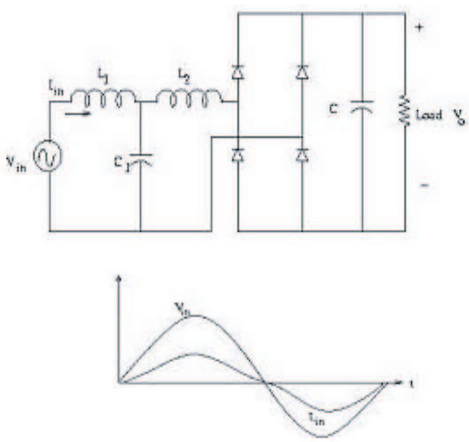

Figure 1: Passive PFC technique.

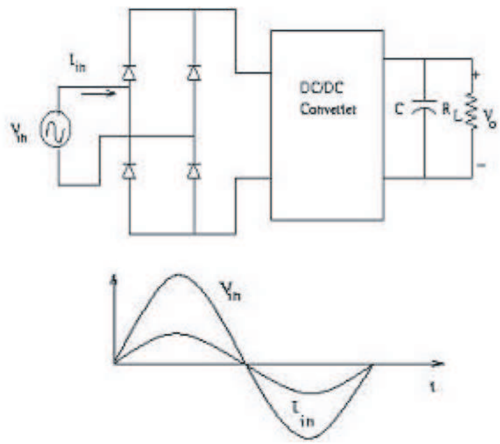

Figure 2: Active PFC technique.

The active PFC techniques can be classified as:

(1) PWM power factor correction techniques

(2) Resonant power factor correction techniques

(3) Soft switching power factor correction techniques

In PWM power factor correction approach, the power switching device operates at pulse-width-modulation mode. Basically in this technique switching frequency of active power switch is constant, but turn-on and turn-off mode is variable. The advantages are simple configuration, ease of analysis and control, lowest voltage and current stress. Therefore it is extensively used in PFC circuits. For the minimization of converter size PWM technique generates significant switching loss [1].

Different topologies of PWM techniques are as follows:

(1) Buck type

(2) Flyback type

(3) Boost type

(4) Cuk' type

Figure 3 shows the buck type topology. The advantage of buck type topology is that the converter can supply a low output voltage with respect to input voltage. The disadvantages are, significant current distortion, EMI is higher because discontinuous input current so filter design is costly. It is a basic DC-DC converter and it is not used for power factor correction [1].

Figure 4 shows the flyback type topology. Its advantages are, output voltage can be higher or lower than input voltage and input and output can be isolated. The disadvantages are higher switching device voltage and current rating, input current is discontinuous so requirement of careful design of input filter, difficult to program the input current with current mode control [1].

The boost type topology is shown in Figure 5. Advantages of this topology are current mode control is easy and less EMI so reduced input filtering requirements. The main disadvantages are more conduction loss, no isolation and output voltage is always higher than input voltage [1].

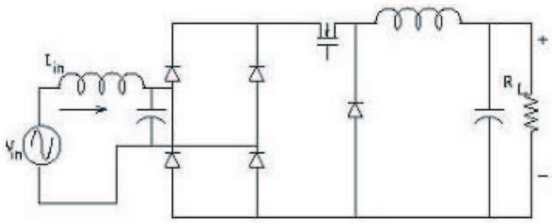

Figure 3: Buck type topology.

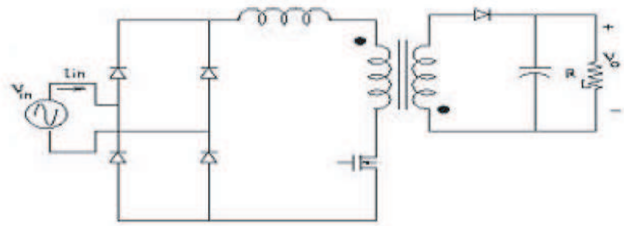

Figure 4: Flyback type topology.

The Cuk' type is shown in Figure 6. The advantages are, input current is remain continuous even if the converter operates in discontinuous conduction mode, and output voltage can be lower or higher than the instantaneous input voltage. The disadvantages are the increased voltage and current stress on power devices, requirement of extra inductor and capacitor and isolation is not provided [1].

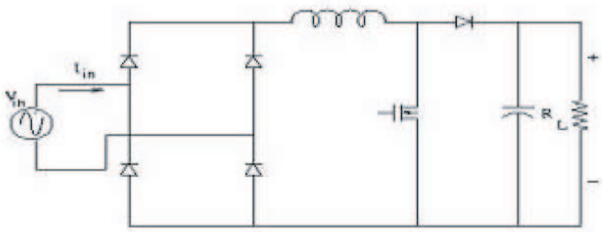

Figure 5: Boost type topology.

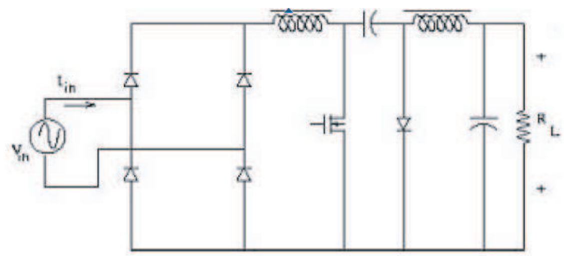

Figure 6: Cuk' type topology.

In the resonant converter, the voltage across a switch or the current through a switch is shaped by the resonance of inductor and capacitor to become zero at the time of turned on or off. Thus the switching loss is greatly reduced. The high power factor is achieved by the natural gain-boosting characteristic of the resonant converter. The major drawbacks are higher voltage and current stress on the power switch with respect to PWM mode and variable switching frequency employed. Figure 7 shows a PFC circuit in which a resonant converter is inserted between the input diode rectifier and the dc-dc converter. This resonant converter can be series resonant converter or a charge pump resonant network [3]. The advantage is that the current stress and voltage stress on resonant components as well as power switches are lower than the previous resonant converter [1].

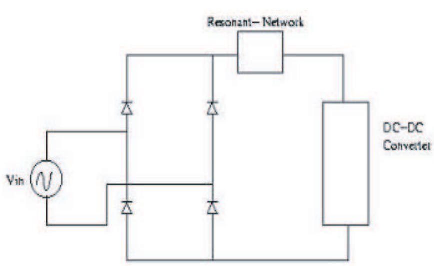

Figure 7: Resonating PFC circuit.

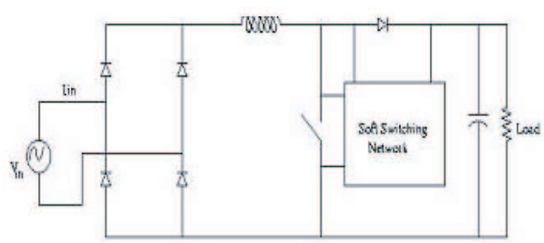

Figure 8: Soft switching PFC circuit.

The soft-switching PFC technique combines the advantages of PWM mode and resonant mode techniques with an additional resonant network consisting of a resonant inductor, a resonant capacitor and an auxiliary switch. The AC/DC converter operates in PWM mode during most portion of a switching cycle but operates in resonant mode during the switch turn-on and turn-off intervals. As a result, the PFC circuit works at constant switching frequency and the power switch turns on and off at zero current or zero voltage conditions. Thus efficiency and power factor both improved by this technique. Figure 8 shows boost PFC circuit with a soft switching network [1].

3. Single Phase Active Power Factor Correction

Conventional off-line power converters with diode capacitor rectifier front-end have distorted input current waveform with high harmonic content. They cannot meet neither the European line-current harmonic regulations defined in the IEC1000-3-2 document nor the corresponding Japanese input-harmonic current specifications. To meet the requirements of above norms it is customary to add a power factor corrector ahead of the isolated dc/dc converter section of the switching power supply. Again another dc/dc converter is needed for output voltage regulation. Thus there are two converter is needed for single-phase active power factor correction for the requirement of high input power factor and tight output regulation. There are two approaches for single-phase active power factor correction:

(1) Two-stage approach

(2) Single-stage approach

Two-stage approach is commonly used approach in high power applications [4]. The block diagram of two stages PFC converter is shown in Figure 9. In this approach, there are two independent power stages. The front-end PFC stage is usually a boost or buck-boost (or flyback) converter. The dc/dc output stage is the isolated output stage that is implemented with at least one switch, which is controlled by an independent PWM controller to tightly regulate the output voltage. The two-stage approach is a cost-effective approach in high power applications; its cost-effectiveness is diminished in low-power applications due to the additional PFC power stage and control circuits.

A single-stage scheme combines the PFC circuit and dc/dc power conversion circuit into one stage. A number of single-stage circuits have been reported in recent years. Figure 10 shows the block diagram of single-stage approach. Compared to the two-stage approach, the single approach uses only one switch and controller to shape the input current and to regulate the output voltage. Although for a single-stage PFC converter attenuation of input-current harmonics is not as good as for the two-stage approach. But it meets the requirements of IEC1000-3-2 norms. Again it is cost effective and compact with respect to two stage approach [4].

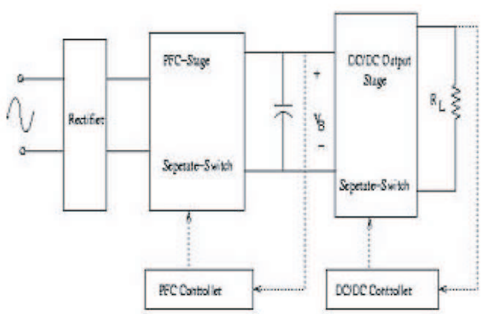

Figure 9: Block diagram of two stage approach.

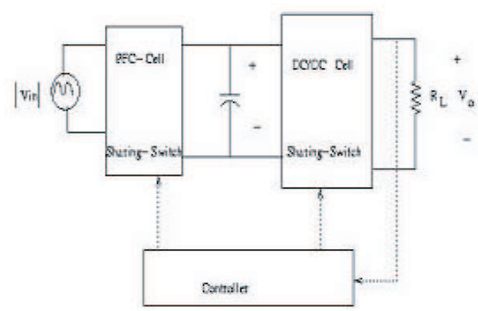

Figure 10: Block diagram of single stage approach.

There are four possible combinations to obtain different single stage single switch PFC converters [5]:

(1) Discontinuous Conduction Mode PFC + Continuous Conduction Mode DC/DC

(2) Discontinuous Conduction Mode PFC + Discontinuous Conduction Mode DC/DC

(3) Continuous Conduction Mode PFC + Continuous Conduction Mode DC/DC

(4) Continuous Conduction Mode PFC + Discontinuous Conduction Mode DC/DC

4. Direct Power Transfer Scheme

Either in two-stage or single-stage of single phase PFC the input power is processed twice to reach the output. There are two functional cells known as PFC cell and DC/DC cell is used for power factor correction and output voltage regulation respectively. Figure 11 shows the power processing in typical single-phase single-stage approach by block diagram. Suppose efficiency of PFC cell is η_1 and DC/DC cell is η_2 than the output power will be

$$P_0 - P_{\text{in}}\eta_1\eta_2 \tag{1}$$

Thus the efficiency of single-stage AC/DC converter will be,

$$\eta = \eta_1\eta_2 \tag{2}$$

Thus the twice power processing approach means low conversion efficiency because it is a product of two fraction. So, advancement is needed for the improvement of conversion efficiency.

The proposed approach come into picture according to that, it is not necessary to process all input power twice to achieve well-regulated and high input power factor DC output power. In this approach some power is

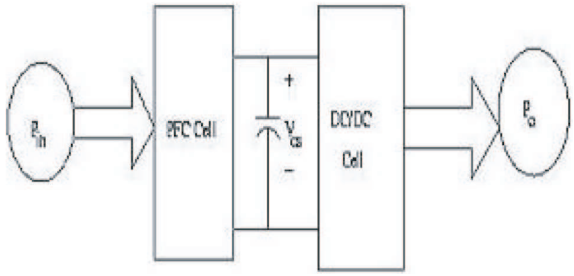

Figure 11: Conventional single stage approach.

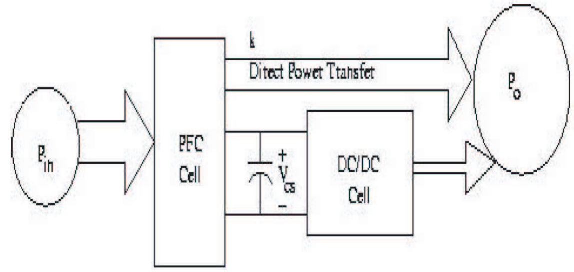

Figure 12: Proposed DPT scheme.

processed only once and remaining power processed twice to keep the total DC output power constant. Figure 12 shows the proposed new direct power transfer scheme. For this kind of power transfer, with whom some power is processed only once is called direct power transfer (DPT) scheme [6].

Let k portion of power from PFC cell be directly transferred to output, and remaining (1-k) power from PFC cell is stored in intermediate bus capacitor and then processed by DC/DC cell. Based on the proposed concept, output power can be obtained by Eq. (4), (3).

$$P_0 = P_{\text{in}}\eta_1\eta_2(1-k) + P_{\text{in}}\eta_1 k \tag{3}$$

Thus efficiency of proposed direct power transfer scheme single-stage PFC AC/DC converter is,

$$\eta = \eta_1\eta_2 + k(1-\eta_2)\eta_1 \tag{4}$$

Comparing Eq. (2) and Eq. (4), it is easy to say efficiency of DPT scheme is more than the efficiency of conventional single-stage scheme.

5. Direct Power Transfer Topology

The proposed DPT topology integrates flyboost PFC cell in existing single stage DC/DC cell. All the derived topologies are differentiated by only application of DC/DC cell. Different DC/DC cells are used for improving voltage regulation and reducing DC bus stress. Power unbalance between PFC stage and dc/dc stage is the inherent reason for causing high DC bus voltage stress. In order to meet the criteria of low DC bus voltage DC/DC cell used in this converter is work on the concept of "series charging, parallel discharging capacitors scheme (SCPDC)" [5]. The SCPDC means that the two energy-storage capacitors are charged in series when the switch is off and discharged in parallel when switch is on.

This topology integrates one parallel PFC cell and one parallel-series forward DC/DC conversion cell. Parallel PFC cell is basically a flyback transformer and integration of boost features. For achieving high power factor PFC block should work on DCM. Figure 13 shows the laboratory type AC/DC converter. Flyboost part is already explained in section 4.2. Here main difference in flyboost part of previous topology is unbalanced power is controlled properly, so DC bus voltage is less compared to other topologies of single stage single switch AC/DC converter.

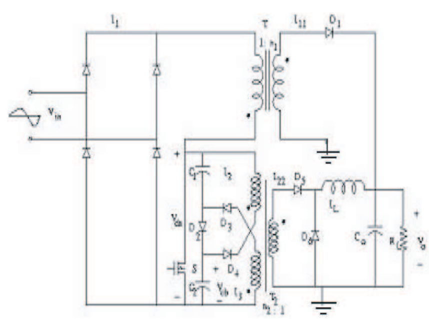

Figure 13: Proposed AC/DC converter.

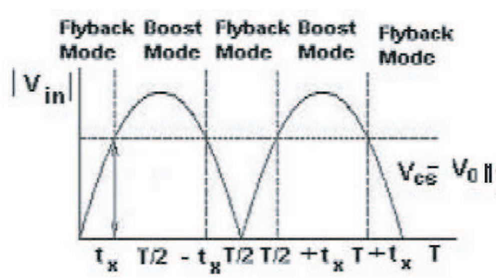

Figure 14: Modes of operation.

Parallel PFC cell contains; transformer T_1, input bridge rectifier, two intermediate bus capacitors, diode D_1 and diode D_2, and active switch S. The parallel-series forward DC-DC conversion cell contains, forward transformer T_2, output inductor L_o, output capacitor C_o, and also bus capacitors, diodes, switch. Thus both cells share bus capacitors, the only active switch and controller. Same as other single-stage PFC topologies the two cells are operate independently. But the operation of this topology differs in other topologies in terms of

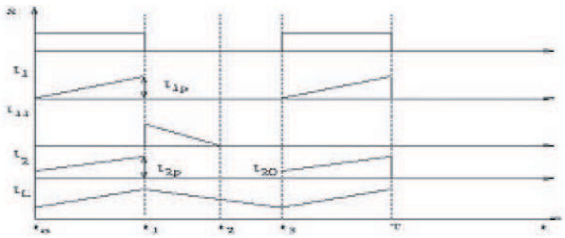

Figure 15: Flyback mode of operation.

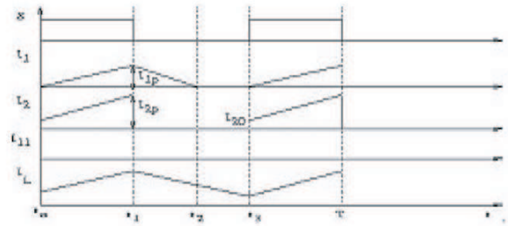

Figure 16: Boost mode of operation.

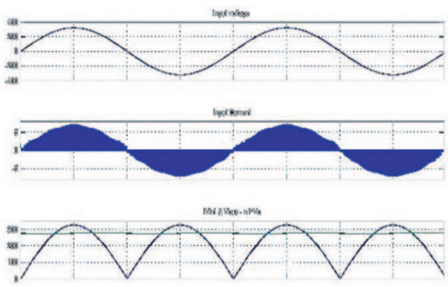

Figure 17: Waveforms of input voltage, input current and modes of operation.

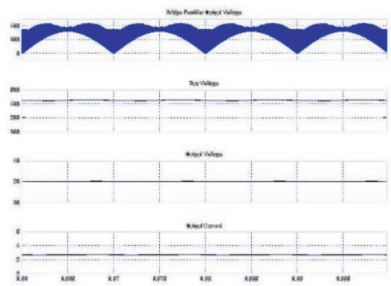

Figure 18: Waveforms of bus voltage, output voltage and current.

parallel power flow nature and special mode of operation. For low input voltage, works as a flyback transformer and at the high input voltage works as a boost inductor.

Modes of Operation: PFC cell works in two modes of operation. The following discussion explains the modes of operation.

Suppose diode D_1 is conducting, applying KVL for primary side

$$|V_{\text{in}}(t)| = V_o/n_1 + V_{D2} + V_{cb}$$

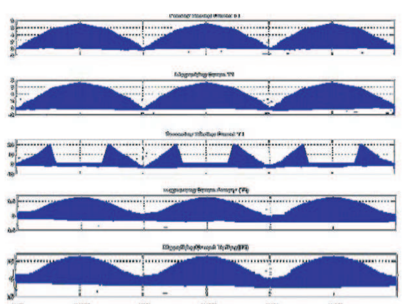

Figure 19: Waveforms of current of transformer T_1 and T_2.

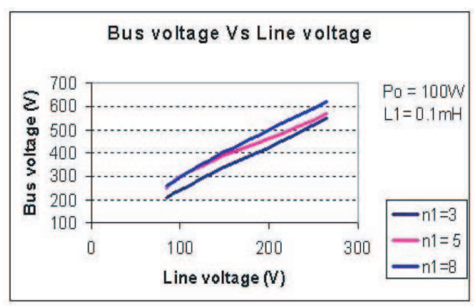

Figure 20: Bus voltage versus line voltage.

Where $V_{\text{in}}(t)$, is input voltage, V_o the output voltage, n_1 the turn ratio of transformer T_1, V_{cb} the voltage across bus capacitor and V_{D2} the voltage across diode D_2.
So, $V_{D2} = |V_{\text{in}}(t)| - (V_{cb} - V_o/n_1)$
For D_2 to be conducting the condition is;

$$|V_{\text{in}}(t)| \geq (V_{cb} - V_o/n_1) \tag{5}$$

Now suppose diode D_2 is conducting, the reflected voltage on secondary side will be;

$$[|V_{\text{in}}(t)| - V_{cb}]n_1$$

Applying KVL on secondary side

$$[|V_{\text{in}}(t)| - V_{cb}]n_1 + V_{D1} + V_o = 0$$

Where, V_{D1} is the voltage across diode D_1. For D_1 to be conduct V_{D1} should be greater or equal to zero, so the condition is;

$$|V_{\text{in}}(t)| \leq (V_{cb} - V_o/n_1) \tag{6}$$

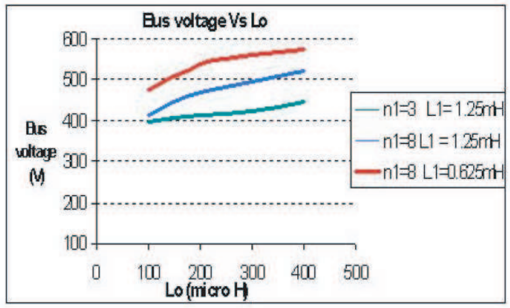

Figure 21: Bus voltage versus output inductance.

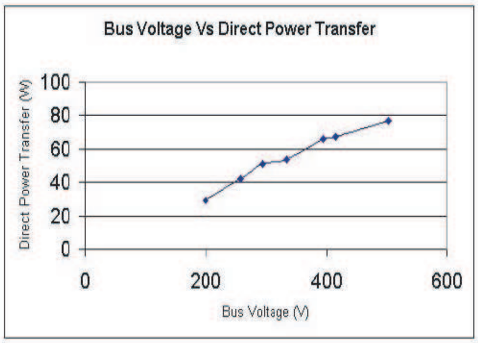

Figure 22: Bus voltage versus DPT.

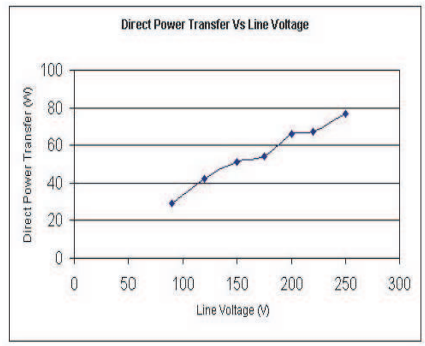

Figure 23: DPT versus line voltage.

From the Eq. (5) and Eq. (6) it is clear that the diode D_1 and the diode D_2 do not conduct simultaneously. So, when D_1 will conduct D_2 will not conduct vice-versa. Thus there are two modes of operation. Figure 14 shows the operation modes of flyboost PFC cell.

Thus there are two modes of operation:

(1) Flyback Mode

(2) Boost Mode

Flyback Modes of Operation: it is easy to understand for the interval when line voltage $|V_{in}(t)|$ is less than $V_{cb} - n_1V_o$ transformer T_1 work as a flyback transformer. It discharges all its energy directly to the load. Thus power transferred directly. This portion of power is processed by active switch only once. At the same time DC/DC cell will deliver some power from bus capacitors to the load to improve output voltage regulation. Operational waveform in this mode is shown in Figure 15. There are three interval of operation in flyback mode.

(1) First Interval: When switch is on at t_o rectified line voltage is applied to the transformer T_1. Transformer T_1 work as a flyback transformer. Power is transferred to the load at the time when switch is off. The bus capacitors voltage is applied to the inductor through the transformer T_2 for the regulation of output voltage. The special configuration of parallel-series forward conversion cell is useful for controlling DC bus voltage.

(2) Second Interval: When switch is turned off at t_1, energy is transferred by transformer T_1 to the load so voltage across T_1 will be n_1V_o. Freewheeling path of diode D_6 is through output inductor L_o. Transformer T_2 resetting its energy through bus capacitors by the help of diodes D_2–D_4. Voltage across switch is clamped to sum of capacitors, C_1, C_2 voltage. Thus the switching voltage is reduced by this configuration.

(3) Third Interval: At t_2 all magnetizing energy of transformer T_1 is transferred to the load. Now the current of secondary winding of transformer will be zero. Transformer T_2 continues to reset through the bus capacitors, since it is fixed to bus voltage.

Boost mode of operation: When line voltage $|V_{\text{in}}(t)|$ is higher than $V_{cb} - n_1V_o$ transformer T_1 works like a boost inductor. All magnetizing energy of both bus capacitors is discharged via D_2 and DC-DC cell delivers all output power from bus capacitors to the load. Thus power processing two times by the active switch. The operational waveform is shown in Figure 16. Circuit operation in this mode is same as flyback mode in the first and third interval. But for the second interval it is different. In the second interval primary current of transformer T_1 will decrease. The current of output inductor freewheels through diode D_6. Transformer T_2 is resetting through diode D_3–D_4. The transformer action of flyback transformer is not working. This is due to reverse biased nature of flyback transformer diode D_1. Therefore output current of secondary transformer is zero in this mode.

6. Simulation Results

The circuit shown in Figure 13 has been simulated in Matlab, the simulation results is shown in Figures 17, 18 and 19. The operating switching frequency is 50 kHz. As Figure 17 shows the input current tracks the input voltage so input power factor is almost unity. The two modes of operation, flyback mode and boost mode are clearly specified in Figure 17. As shown in Figure 18, bus voltage is fixed at 420 V; so switching stress is not high. Output voltage is almost fixed at 30 V, so it is well regulated. Simulation is done for 100 W AC/DC converter.

The Figure 19 shows currents in different cells. As the requirement is PFC cell works on DCM mode and DC-DC cell works on CCM mode, it is clearly specified in Figure 19. Secondary winding current of flyback transformer carry current only in flyback mode, in boost mode primary winding of flyback transformer works as a boost inductor.

Figure 20 shows bus voltage versus line voltage at different turns ratio. As turns ratio of transformer T_1 increases bus voltage increases almost linearly.

Figure 21 shows DC bus voltage output inductance value of forward DC-DC cell. As output inductance increases DC bus voltage increases. Again it is a function of turn ratio of flyback transformer, higher the turn ratio lowers the flyback mode, lower the direct power transfer and so lower the efficiency. But small turns ratio will results in very low bus voltage, which may cause PFC cell to operate under CCM. Since there is no active control over PFC cell, it will cause very high peak current. So, it limits the minimum turns ratio value. Hence, in order to achieve lower bus voltage, L_1 should be as large as possible, while n_1 and L_o should be as small as possible.

Figures 22 and 23 shows the direct power transfer versus bus voltage and line voltage. Higher the line voltage and bus voltage higher will be the direct power transfer.

7. Conclusion

From above discussions in this paper, it is clear that the power factor correction is being given significant importance for low power applications. Also as power electronic equipments are increasingly being used, they pose a serious problem of low order harmonics on utility side. Among various schemes available for PFC, the single stage scheme is best suited for low power application because of its cost effectiveness. But in this scheme, there is a serious limitation of high dc link voltage rise under light load condition. This problem can be addressed by using the concept of Direct Power Transfer. From the simulation and experimental results of DPT topology, it is clear that DPT is an effective way to control high dc link voltage and hence reduces the component stresses. This topology also maintains a good source power factor and a tight output voltage regulation without compromising with high DC bus voltage. Moreover, the efficiency of overall power conversion is high.

REFERENCES

1. Mohan, N., T. M. Undeland, and W. P. Robbins, *Power Electronics, Converters, Applications, And Design*, 2nd Edition, John Wiley and Son, Inc., New York, 1995.
2. Yang, Z. H. and P. C. Sen,, "Recent developments in high power factor switch -mode converters," *IEEE Canadian Conference on*, Vol. 2, 477–488, May 1998.
3. Qian, J. R. and F. C. Lee, "Charge pump power-factor-correction technologies. i. concept and principle," *IEEE Transaction on Power Electronics*, Vol. 15, 121–129, Jan 2000.
4. Zhang, J. D., M. M. Jovanovic, and F. C. Lee, "Comparison between CCM single-stage and two-stage boost PFC converters," *APEC 1999*, Vol. 1, 335–341, March 1999.
5. Luo, S. G., H. Wei, G. Y. Zhu, and I. Batarseh, "Several schemes of alleviating bus voltage stress in single stage power factor correction converters," *PEDS 1999*, Vol. 2, 921–926, July 1999.
6. Luo, S. G., W. H. Qiu, W. K. Wu, and I. Batarseh, "Flyboost powers factor correction cell and its applications in single-stage AC-DC converters," *PESC 2002*, Vol. 3, 1375–1380, June 2002.

A New Generalized Space Vector Modulation Algorithm for Neutral-point-clamped Multilevel Converters

P. Purkait and R. S. Sriramakavacham
Birla Institute of Technology, India

Abstract—Neutral-point-clamped converters are increasingly applied in industrial drive systems as they allow the use of lower voltage devices in higher voltage applications, provide reduced output voltage total harmonic distortion(THD), and can develop low common mode voltage. Several distinct modulation strategies have been proposed in the past for eliminating the common mode voltage, providing low THD output voltage or reducing the neutral point current ripple. However each of these strategies improves the performance of the converter in one view point while losing performance in the other view point. A new generalized space vector modulation technique is proposed. Analytical model and simulation results are presented.

1. Introduction

In recent years, industry has begun to demand higher power equipment, which now reaches the megawatt level. Controlled ac drives in the megawatt range are usually connected to the medium voltage network. Today it is hard to connect a single power semiconductor switch directly to medium voltage grids. For these reasons, a new family of multilevel inverters came as the solution for working with higher voltage levels. In particular, they provide low line voltage dv/dt and improved spectral characteristics of the output signals. The three level neutral-point-clamped (NPC) converters are used widely in adjustable speed a.c drive systems, providing less stress on motor winding, insulation and bearings. It is leading to an increase of the reliability and the life period of the drive systems.

Several carrier-based and space vector modulation strategies have been proposed for these converters [7]. These algotithms were designed to provide adjacent state switching action in the converter which yields the lowest possible output voltage and current total harmonic distortion. The most significant advantages of SVPWM are fast dynamic response and wide range of fundamental voltage compared with the conventional PWM. But when it is applied to the diode-clamped converter, the SVPWM strategy also has to solve the neutral-point voltage un-balance problem.

There are three main steps to obtain the proper switching states during each sample period for the SVPWM method:

1. Choose proper basic vectors.
2. Calculation of dwelling time of selected vectors.
3. Selection of proper sequence of pulses.

One way for calculating the time is to decompose all the vectors into real and imaginagy part [1]. Another way is to calculate the time according to reference voltage vector of each phase [3, 2].

To solve the problem of computational complexity in multilevel converter due to large number of redundant switching states, a new generalized space vector algorithm is proposed. This new space vector strategy eliminates low frequency ripple from the dc link capacitors of a three-level converter. The proposed algorithm for threeClevel converter is verified by simulation and the results are compared with the existing method, nearest three vector algorithm [4].

2. Three-phase Three-level Converter

Figure 1 presents the basic structure of a three-level neutral-point-clamped converter. Each of three legs of the converter consists of four power switches, four freewheeling diodes and two clamping diodes that limit the voltage excursions across each device to half the input dc-bus voltage.

3. Nearest Three Vector Modulation

Table 1 shows the possible switching states for the three level converter of Figure 1. There are nineteen basic space vectors for a three-level converter and they are shown in Figure 2. The zero voltage vector has three switching states (000, 111, -1-1-1). Each of the six small vectors (V_1–V_6) has two switching states and each of the middle vectors (V_8, V_{10}, V_{12}, V_{14}, V_{16}) and the large vectors (V_7, V_9, V_{11}, V_{13}, V_{15}, V_{17}) has one state respectively.

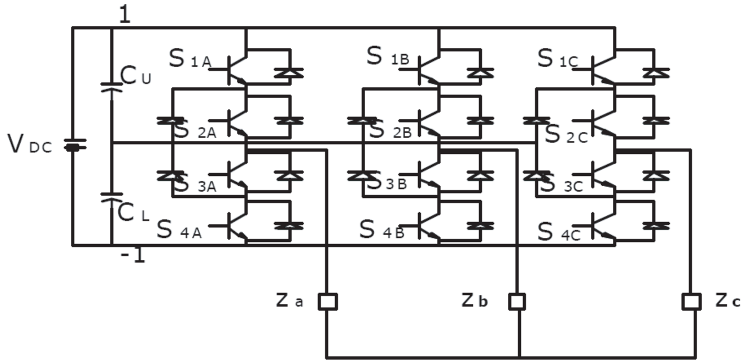

Figure 1: Basic structure of three level diode clamped converter.

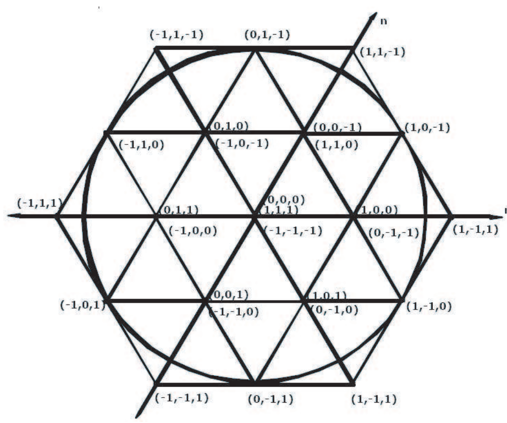

Figure 2: Switching states of converter.

Table 1: Switching states of three-level converter ($X = A, B, C$).

STATUS	S_{1X}	S_{2X}	S_{3X}	S_{4X}
1	ON	ON	OFF	OFF
0	OFF	ON	ON	OFF
-1	OFF	OFF	ON	ON

In SVPWM technique, the reference voltage vector V_r is located in a triangle, in which three voltage vectors are corresponding to the three apexes. They are selected to minimize the harmonic components of the output line voltage.

The dwelling time of each vector should satisfy the following equations:

$$V_1 t_1 + V_7 t_7 + V_8 t_8 = V_r T \tag{1}$$

$$t_1 + t_8 + t_8 = T \tag{2}$$

where T is the sampling period and t_1, t_7 and t_8 are the dwelling time of V_1, V_7 and V_8 respectively.

Following four methods are required in the nearest three vector modulation algorithm to attain the complete switching states for a multilevel converter by using SVPWM.

Step I: Decomposing of Basic Vectors

A new coordinates namely m-n coordinates can be established. The new coordinate have two axes intersecting with the angle of $\pi/3$. Only the first quadrant of the coordinate is used because the vector located in other region can be transformed to the first quadrant by clockwise rotating an angle $K^*(\pi/3)$ where, $K = 1, 2, 3, 4, 5$ for region B, C, D, E and F respectively.

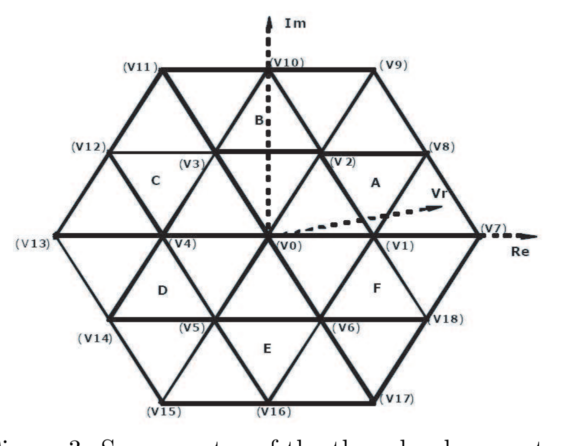

Figure 3: Space vector of the three level converter.

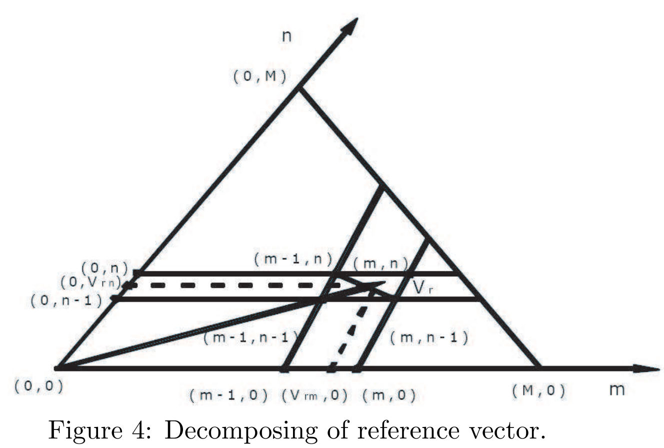

Figure 4: Decomposing of reference vector.

Universally a $(M+1)$ level inverter is discussed here. As shown in Figure 4, the reference vector is decomposing into m-axis and n-axis.

$$V_{rm} = 2MV_r/(\sqrt{3}V_{dc})\sin(\pi/3-\theta) \quad (3)$$
$$V_{rn} = 2MV_r/(\sqrt{3}V_{dc})\sin(\theta) \quad (4)$$

Step II : Selecting Three Nearest Vectors

Considering that following inequalities are satisfied by V_{rm} and V_{rn}

$$(m-1) < V_{rm} < m \quad (5)$$
$$(n-1) < V_{rn} < n \quad (6)$$

where m and n are integers. There are three possible cases:

1. $V_{rm}+V_{rn} < (m+n-1)$: That means V_r is located in the left bottom shadow triangle. The vectors $(m-1,n-1)$, $(m-1,n)$ and $(m,n-1)$ are the nearest vectors.
2. $V_{rm}+V_{rn} > (m+n-1)$: That means V_r is located in the right top shadow triangle. The vectors $(m-1,n)$, $(m,n-1)$ and (m,n) are the nearest vectors.
3. $V_{rm}+V_{rn} = (m+n-1)$: V_r lies at the middle line and either 1. or 2. can be choosen.

Step III : Dwelling Time Calculation

Dwelling time calculation is given here. Taking $(m1,n1)$, $(m2,n2)$ and $(m3,n3)$ are three nearest vector. Corresponding dwelling time can be calculated from the following equations.

$$m_1t_1+m_2t_2+m_3t_3 = V_{rm}*T \quad (7)$$
$$n_1t_1+n_2t_2+n_3t_3 = V_{rn}*T \quad (8)$$
$$t_1+t_2+t_3 = T \quad (9)$$

Step IV : Neutral Point Potential Control

It is very important to balance neutral point potential. For balancing neutral point potential selection of proper switching sequence is necessary. For example, when V_r falls in the triangle formed by the apexes of vectors V_1, V_7 and V_8, the switching sequence can be selected as (100) - (10-1) - (00-1) - (0-1-1) or (110) - (100) - (10-1) - (00-1). The two sequences lead to the same output voltage but have the opposite effect on the neutral point voltage.

Over Modulation Control

However, there is one exception when the reference voltage vector lies outside the hexagon. In this case, the over modulation mode occures and the output line voltages distort.

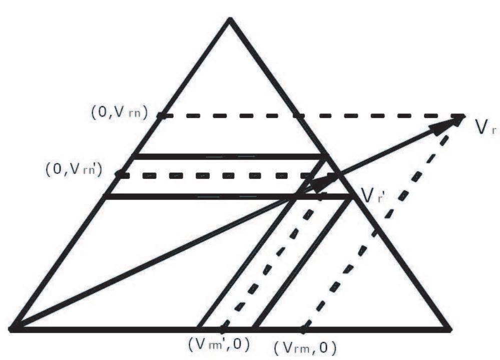

Figure 5: Over modulation control.

Following algorithm can be used when reference vector lies in the over modulation region,

$$\text{If } (V_{rm}+V_{rn}) > M$$

$$V_{rm'} = V_{rm}*M/(V_{rm}+V_{rn}) \quad (10)$$
$$V_{rn'} = V_{rn}*M/(V_{rm}+V_{rn}) \quad (11)$$

4. New Space Vector Modulation Algorithm

It has been shown that switching states where the three ac terminals are connected to the three different voltage level of dc bus are the primary cause of increased harmonic content in the dc bus currents. The presence of significant third harmonic content in the neutral point current causes a significant sizing penalties on the dc link capacitor of three level converter [6]. A new space vector modulation algorithm is proposed to eliminate the harmonic content in neutral current.

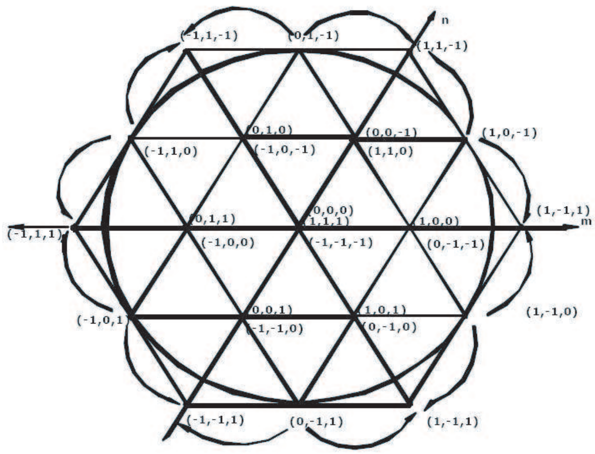

Figure 6: Redistribution of switching states in R.S.S. algorithm.

It can be deduced that the identical voltages can be generated if the duty cycle of these state is equally divided between two states that are adjacent to it and lie on the same hexagonal plane. Figure 6 shows the redistribution of switching states.

As an example, redistribution of dwelling time in Figure 6 for (1,-1,-1), (1,1,-1) and (1,0,-1) can be done as follows,

$$t_{1,-1,-1} = t_{1,-1,-1} + (t_{1,0,-1}/2) \tag{12}$$

$$t_{1,1,-1} = t_{1,1,-1} + (t_{1,0,-1}/2) \tag{13}$$

$$t_{1,0,-1} = 0 \tag{14}$$

Though we have eliminated six switching states still DC-bus utilization factor in this method is identical with nearest three vector modulation, as the hexagon and inscribe circle are equal.

5. Simulation Results

Extensive MATLAB/SIMULINK models of three level inverter systems were developed for analysing the nearest three point modulation and new proposed method on output line voltage and neutral point current.The simulation of threeClevel converter shown in Figure 1 was done under the conditions listed in Table 2.

Table 2: Simulation conditions.

Sampling Time	50 μSec.
DC Link Voltage	400 Volts
Active Load	1 KW
Reactive Power (-ve)	500 VAR
Output Frequency	50 Hz
Modulation Index	0.7

1. Output Line Voltage

Figure 7 and Figure 9 are the line-line voltage of nearest three vector modulation and new proposed approach respectively. The FFT analysis (Figure 8 and Figure 10) of both the line-line voltages are also shown.

2. Line Current

Figure 11 and Figure 13 are the line currents of nearet three vector modulation and new proposed approach respectively and their FFT analysis also shown in Figure 12 and Figure 14.

3. Neutral Point Current

FFT analysis of neutral current of nearet three vector modulation and new proposed approach are shown in Figure 15 and Figure 16 respectively. New proposed method eliminates the harmonic content in neutral point current while the nearest three vector method shows harmonics in neutral point current.

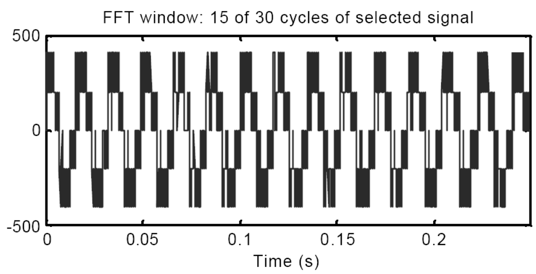

Figure 7: Line-line voltage.

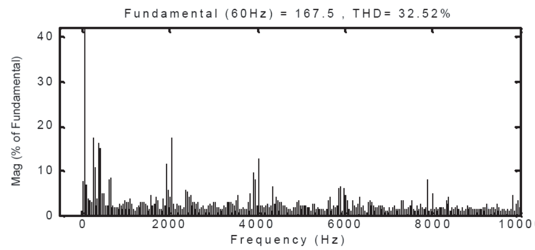

Figure 8: FFT analysis of line-line voltage.

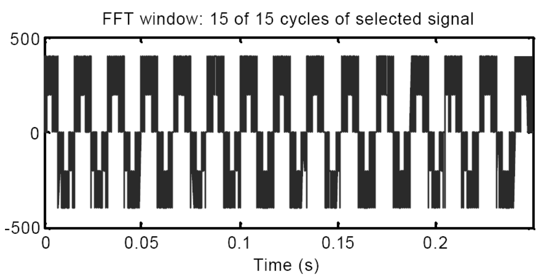

Figure 9: Line-line voltage waveform.

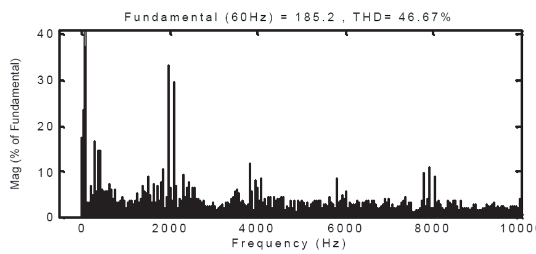

Figure 10: FFT analysis of line-line voltage.

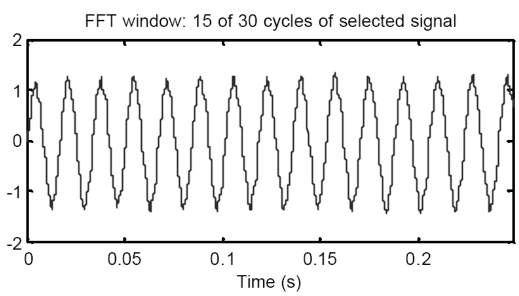

Figure 11: Line current waveform.

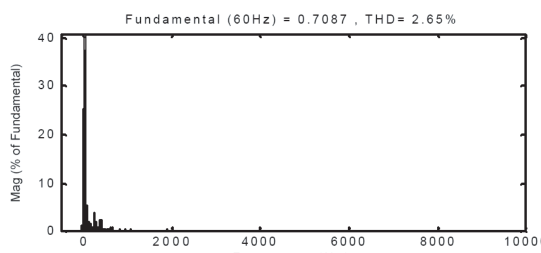

Figure 12: FFT analysis of line current.

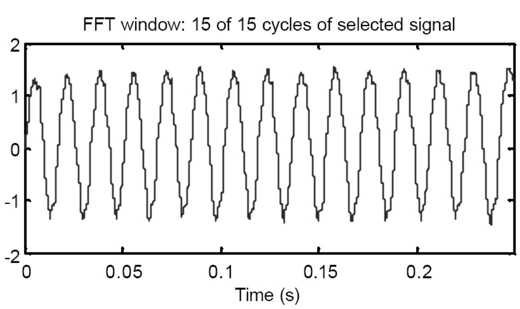

Figure 13: Line current waveform.

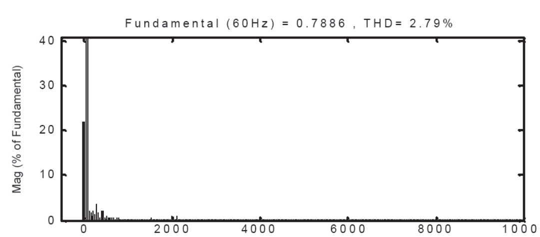

Figure 14: FFT analysis of line current.

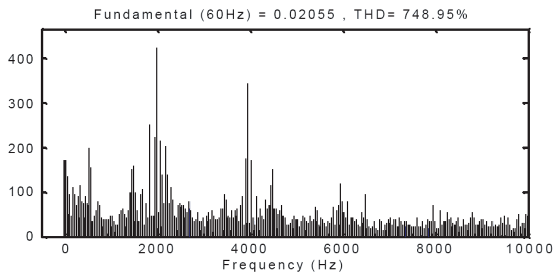

Figure 15: FFT analysis of neutral current.

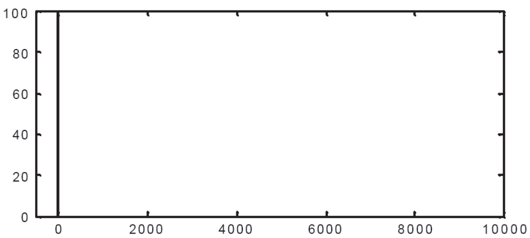

Figure 16: FFT analysis of neutral current.

6. Conclusion

A new simple SVPWM method is proposed and verified by simulation of three-level-inverter. If number of levels increases more complexity will come in the proposed method while algorithm will be same. This paper presents a new way of implementing the proposed space vector modulation algorithm for reducing the neutral point current in the multilevel inverter.

From the FFT analysis of line voltage and neutral current it is concluded that

1. Low frequency harmonic content of the neutral current is zero.
2. Neutral point current has a zero d.c average value.
3. Line voltage contains slightly larger harmonics in proposed method with respect to nearest three vector modulation.

REFERENCES

1. Seo, J. H., C. H. Choi, and D. S. Hyun, "A new simplified space-vector PWM method for three-level-inverters," *IEEE Trans. Power Electronics*, Vol. 16, 527–534, July 2001.
2. Maruyama, T., M. Kumano, and M. Asish, "A new asynchronous PWM method for a threelevel-inverter," *Conf. Rec. 1991 IEEE Int. Power Electronics Specialists Conf.*, 366–371, 1991.
3. Seo, J. H. and C. H. Choi, "Compensation for the neutral-point-potential variation in three-level-space-vector PWM," *Conf. Rec. 2001 IEEE Int. Applied Power Electronics Conference and Exposition*, Vol. 2, 1135–1146, 2001.
4. Hu, L., H. Y. Wang, Y. Deng, and X. N. He, "A simple SVPWM algorithm for multilevel inverters," *2004 35th Annual IEEE Power electronics Specialist Conference*, 3476–3480, 2004.
5. Bendre, A., S. Krstic, J. V. Meer, and G. Venkataramanan, "Comparative evalution of modulation algorithms for neutralpoint-clamped converters," *IEEE Transaction on Industry Applications*, Vol. 41, No. 2, March/April 2005.
6. Bendre, A. and G. Venkataramanan, "Radial space vector modulation—a new space vector technique for reducing dc link capacitor harmonic currents in three-level-converters," *Conf. Rec. IEEE-IAS Annu. Meeting*, Vol. 1, 684–691, 2003.
7. Rodviger, J., J.-S. Lai, and F. Z. Leng, "Multilevel inverters, control and applications," *IEEE Trans on Industrial Electronics*, Vol. 49, No. 4, 724–738, August 2002.

Improved Mesh Conforming Boundaries for the TLM Numerical Method

I. J. G. Scott and D. de Cogan
University of East Anglia, UK

Abstract—The numerical simulation of wave propagation in bounded space using differential-based models generally encounter spatial discretisation problems when the boundaries of the computation space do not fall on exact multiples of the models discretisation. While the accuracy can be improved by refinement of the model, the computational load can increase exponentially, often making the problem unsolvable. There have been some previous attempts to achieve boundary conforming meshes for the TLM numerical method. This paper describes a novel approach which compares well with these methods with a significantly reduced computational load.

1. Introduction

While the Transmission Line Matrix (TLM) numerical method is becoming increasingly easy to utilise for a wider variety of electromagnetic problems, in part, due to the definition of perfectly matched loads (PMLs) [1–3], boundary conforming schemes often increase the computational load and/or complexity of the algorithm, making TLM difficult to implement for simulations of bounded regions that fluctuate rapidly along the periphery (Figure 1(a)). The dotted lines show the sections that will require extra analysis in order to meet with the boundary. While some TLM simulations can be approximated reasonably accurately with a stepped formulation (by extension/deletion of the dashed sections), in the case of most TLM simulations the errors introduced are unacceptable and refinement of the mesh is often performed, increasing both time and memory requirements. If the true distance, l_a in figure lb could be incorporated within the simulation, the mesh would pertain much more closely to the true boundary/surface of the device being modelled.

The length of the transmission line in the TLM algorithm cannot simply be adjusted. As can be observed from Figure 1(b), a signal travelling along the full length ($\Delta x/2$, where Δx is the spatial discretisation in the model), will, after reflecting from the surface, appear back at the boundary adjacent node at time $(k+1)\Delta t$, the same signal travelling along the line of length l_A will appear back at the boundary adjacent node at a time less than $(k+1)\Delta t$, but greater than $k\Delta t$ (where k is the current iteration (discrete time step) and $k+1$ is the succeeding iteration). As propagating signals in TLM must all arrive in steps of the same discretised time (Δt), this cannot be modelled directly.

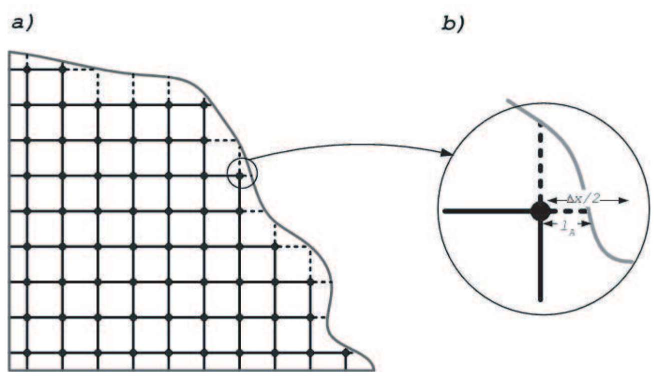

Figure 1: a) Cartesian mesh of non-stepped boundary, b) boundary adjacent node.

De Cogan and de Cogan [4] have adapted existing schemes to demonstrate the application of boundary-conforming finite difference schemes for the solution of the Laplace equation. In a uniformly bounded space where h is the length of the line segments (Figure 2) we use

$$T(x+h,y)+T(x,y+h)+T(x-h,y)+T(x,y-h)+4T(x,y)=0 \tag{1}$$

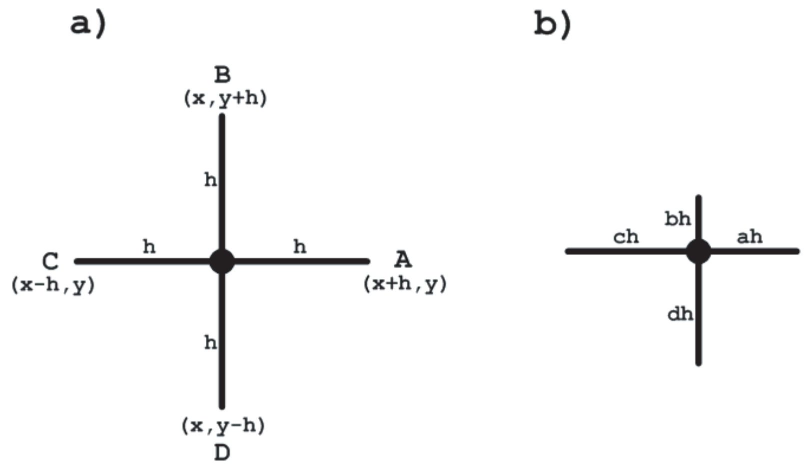

Figure 2: a) 2D FDTD visual representation, b) 2D FDTD irregular boundary visualisation.

In the situation where we take account of a node where we have unequal distances between nodes, given by ah, bh, ch and dh (h is the uniform line-length), the two-dimensional Laplacian becomes

$$\nabla^2 V = \frac{2}{h^2}\left[\frac{V_A}{a(a+c)} + \frac{V_B}{b(b+d)} + \frac{V_C}{c(c+a)} + \frac{V_D}{d(d+b)} - \frac{ac+bd}{abcd}V_0\right] \tag{2}$$

where we consider the potentials of the four nodes, A, B, C, and D which surround the potential V_0.

Using concepts developed in [5] it is easy to see how one might develop a boundary conforming implementation of the wave equation

$$\nabla^2 V = \frac{1}{c^2}\frac{\partial^2 V}{\partial t^2} \tag{3}$$

Although FDTD is well established in electromagnetics and hybrid schemes involving finite difference are well known, there is not much evidence that such a mesh conforming scheme is widely used. Probably because time is implicitly discretised in TLM and because coincidence of arrival is such an important part of TLM algorithms, this subject has received significantly more attention. Early amongst these was the work of Jaycocks and Pomeroy [6]. However, the first really effective technique which was based on firm theoretical foundations was due to Beyer, Mueller and Hoefer [7] and this will hereafter be referred to as the *BMH* method.

This paper will start with a restatement of the BMH method. We will then present our improved formulation which represents a significant improvement in computational efficiency. Analytical results for the horn antenna [8] will be used as a benchmark against which to compare these boundary-conforming schemes against a conventional TLM model with stepped boundaries.

2. Introduction to the BMH Method

The technique proposed in [7] suggests a recursive definition to describe the arbitrary placed boundaries of the mesh. The definition we are interested in here describes an electric wall (reflection coefficient of $\rho = -1$), by adjusting the incident pulses on the line intersected by the boundary. This is given in formula (5) of the BMH paper [7] as:

$$_kV^i = \rho\frac{1-\kappa}{1+\kappa}{}_kV^r + \frac{\kappa}{1+\kappa}(\rho_{k-1}V^r + {}_{k-1}V^i) \tag{4}$$

where $\kappa = 2l/\Delta x$, k is the discretised time step and $_{k-1}V^r\ {}_kV^i$ represent the reflected (scattered) and incident pulses at time $k-1$ and k respectively. Figure 3 illustrates the technique graphically. This approach uses a reference plane located at $\Delta x/2$ from a surface adjacent node (broken line in Figure 3). While this is very effective, there are two important shortfalls. As observed from Figure 3, the bounding wall can only cut the transmission line segment after $\Delta x/2$, if the transmission line is intersected before this, it is necessary to remove the node, extending the line from the previous node, causing κ to become greater than 1. While analysis of this has been performed in [7] ensuring the system remains stable, another error is introduced in the system as the connections between neighbouring nodes are now missing. It appears this does not inhibit the accuracy of the technique as much as a stepped approximation would.

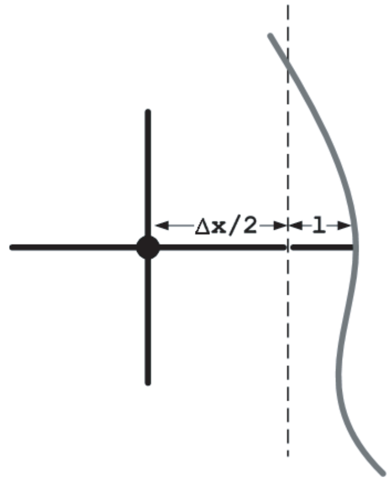

Figure 3: BMH model of arbitrary placed boundary.

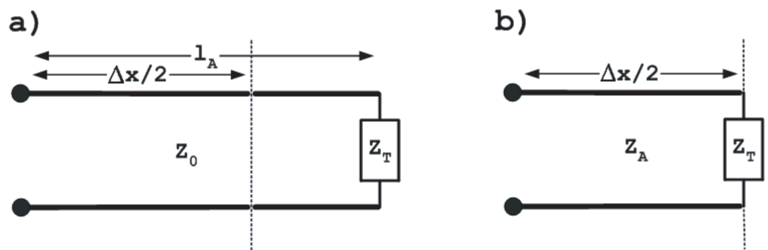

Figure 4: a) Apparent impedance of section of length l_A, b) transformed impedance.

The large memory requirements of the recursive procedure proved particularly limiting in the simulations performed in section 4. For a stepped Cartesian mesh using a scatter-collect type algorithm it is necessary to store only 12 scatter and collect matrices (for the 3D case). To implement (4), a further 8 matrices were required to save the previous scattered and incident pulses. While it is possible to only save the data for the boundary nodes, the complexity of the algorithm is further increased.

3. Improved Conforming Boundary Description

The technique we propose avoids the need for recursion, removing the limitations of the BMH approach, while obtaining results in comparison. We begin with a load termination at some arbitrary non-discrete distance from the $\Delta x/2$ line end (Figure 4(a)). Observing the impedance looking 'down' this line from the node:

$$Z_{obs} = Z_0 \left[\frac{Z_L + Z_0 \tanh(\beta l_A)}{Z_0 + Z_L \tanh(\beta l_A)} \right] \tag{5}$$

where Z_0 is the intrinsic impedance of the line of length l_A, Z_L represents the load impedance, tanh is the hyperbolic tangent function, and $\beta = 2\pi/\lambda$, where λ is the wavelength.

As: $Z_0 = \frac{\Delta t/2}{C_d \Delta x/2} = \frac{\Delta t'}{C_d l_A}$, where $\Delta t'$ is the time a signal takes to traverse the line of length l_A we can replace the line of length l_A, impedance Z_0, with another line of length $\Delta x/2$, with impedance Z_A, as shown in Figure 4(b).

For the case when $\rho = 1$ i. e., $Z_L \to \infty$ Eq. (5) can be simplified to give, after transformation:

$$Z_{obs} = \frac{Z_A}{\tanh(\beta \Delta x/2)},$$

where $\Delta x/2$ is the discretisation of the model.

Assuming low frequencies $\tanh(\beta\Delta x/2) \approx \beta\Delta x/2$. The impedance transformation observed from the node must be the same before and after transformation:

$$\frac{Z_0}{\beta l_A} = \frac{Z_A}{\beta \Delta x/2}$$

hence:

$$Z_A = Z_0 \left[\frac{\Delta x}{2 l_A} \right] \tag{6}$$

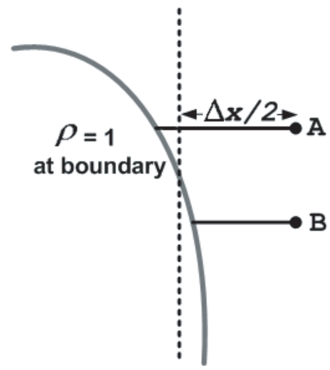

Figure 5: The two cases of impedance transformations covered by (6) and (7).

so if $l_A = \Delta x/2 \quad Z_A = Z_0$
if $l_A > \Delta x/2 \quad Z_A < Z_0$ case A in Figure 5
if $l_A < \Delta x/2 \quad Z_A > Z_0$ case B in Figure 5

Likewise for the case when $\rho = -1$ (i. e., $Z_L \to 0$) (5) simplifies to give, after transformation:

$Z_{obs} = Z_A \tanh(\beta\Delta x/2)$, again assuming $\tanh(\beta\Delta x/2) \approx \beta\Delta x/2$,

Equating before and after transformation:

$$Z_0\beta l_A = Z_A\beta\Delta x/2$$

therefore:

$$Z_A = Z_0\left[\frac{2l_A}{\Delta x}\right] \tag{7}$$

Using both (6) and (7) to describe the boundary adjacent transmission lines for the cases when $\rho = 1$ and $\rho = -1$ respectively, causes the propagating signal to arrive back at the node at time $(k+1)\Delta t$, appearing to have travelled to the true boundary location, while propagating on a line of length $\Delta x/2$.

This scheme will be termed as *uniform* in the analysis performed in section 4.

The nature of mesh-lines at the interface with real surfaces means that we could be dealing with line-lengths in the range $0 < l_A < \Delta x$. Our treatment of this involves expressions with either $\tanh(\beta\Delta x/2)$ or $\tanh\beta\Delta x$. The subsequent analysis assumes that $\tanh\theta \doteqdot \theta$ so that it is sensible to consider the error bands that are involved. In order to reduce the effects of mesh dispersion conventional TLM in two-dimensions is modelled using discretised frequency $\Delta x/\lambda \le 0.1$, which means that we are looking at $\lambda \ge 10\Delta x$. If this is the case then

$$\tanh\beta\frac{\Delta x}{2} = \tanh\frac{2\pi}{\lambda}\frac{\Delta x}{2} = \tanh\frac{\pi}{10}$$

The difference between this and $\pi/10$ is 3.16%, a lower bound.

If $l_A \doteqdot \Delta x$ then our transformation requires that we have $\tanh\beta\Delta x \doteqdot \beta\Delta x$ so that if we persist with $\Delta x/\lambda \le 0.1$ then there is an error of 11.37% in this assumption, an upper bound. We can deduce from this that if we operate at $\Delta x/\lambda \le 0.1/\pi$, then the dispersion at any of the boundary-conforming transmission lines will be no different than if we had used a stepped boundary description with $\Delta x/\lambda \le 0.1$.

4. Comparison of All Techniques

In order to test the accuracy and viability of this technique, an E-plane sectoral horn antenna has been modelled. The analytical solution to describe the radiated fields from the aperture of the horn is described in Balinis [8]. Figure 6 shows the coordinate system used to describe the dimensions of the horn. The field emitted from the E-plane (y-direction in the TLM models) is given as:

$$E_\theta = -j\left(\frac{a\sqrt{\pi\zeta\rho_1}E_1 e^{-j\zeta r}}{8r}\right)\left\{-e^{j(\zeta\rho_1\sin^2\theta/2)}\left(\frac{2}{\pi}\right)^2(1+\cos\theta)F(t_1,t_2)\right\} \tag{8}$$

where ζ denotes the phase factor, E_1 is a constant $F(t_1,t_2) = [C(t_2) - C(t_1)] - j\,[S(t_2) - S(t_1)]$, $C(t_n)$ and $S(t_n)$ denote the cosine and sine Fresnel integrals:

$$C(t_n) = \int_0^{t_n} \cos\left(\frac{\pi}{2}x^2\right) dx, \quad S(t_n) = \int_0^{t_n} \sin\left(\frac{\pi}{2}x^2\right) dx$$

t_n represents:

$$t_1 = \sqrt{\frac{\zeta}{\pi\rho_1}}\left(-\frac{b_1}{2} - \rho_1 \sin\theta\right), \quad t_2 = \sqrt{\frac{\zeta}{\pi\rho_1}}\left(\frac{b_1}{2} - \rho_1 \sin\theta\right)$$

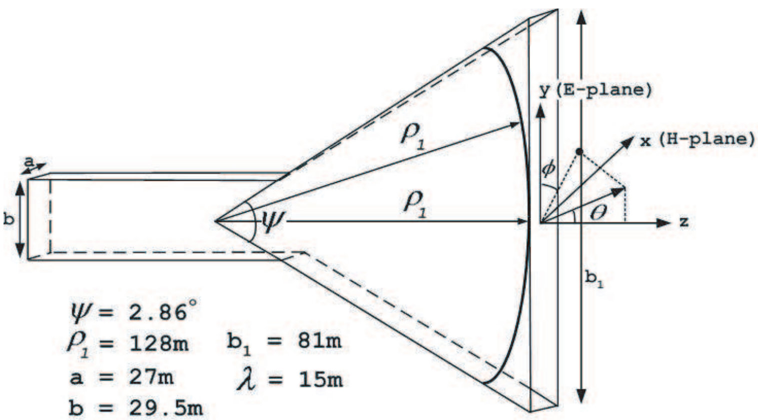

Figure 6: 3D view of E-plane sectoral horn, analytical coordinate system.

Modelling the horn with the dimensions shown in Figure 6, inserting a point source with wavelength of 15 m at the apex of the horn, produces the radiation pattern, along the E-plane, as shown in Figure 7. This has been extracted across the aperture of the horn, from 1/4 into the aperture to 3/4 across (Figure 8), i. e., the centre half of the pattern, this is then plotted over half of the polar diagram. This will act as the benchmark against which to compare the 3D TLM solutions.

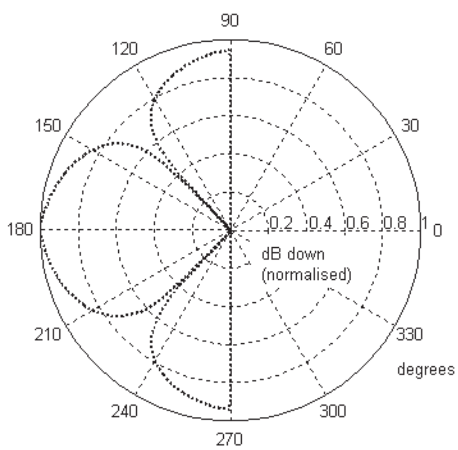

Figure 7: E-plane radiation pattern of E-plane sectoral horn antenna, analytical solution.

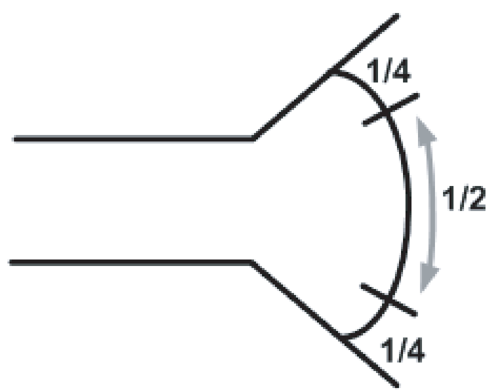

Figure 8: Plotted section of radiated field.

The standard TLM approach creates a 3D Cartesian mesh (for this problem, this is 81 nodes in the north-south direction (y), 128 in the east-west direction (x) and 27 front-back (z)), however as elaborated upon in the discussion given earlier the non-discrete boundaries will become stepped approximations to the true boundary. For this problem the top (south) and bottom (north) boundaries of the mesh will become stepped. The east, west, front and back boundaries are chosen to fall on exact multiples of the models discretisation for the edges of the horn, however to allow the data propagating on the 'corners' of the horn to be included in the simulation, the mouth of the horn has been placed inside the computation space, resulting in east and west boundaries that are also stepped on the flared section of the antennas aperture (Figure 9). Using a reflection coefficient (ρ) of

-1 on all bounding surfaces of the horn and inputting a continuous sinusoidal wave of wavelength 15 nodes (m) at the apex of the horn (marked as ° in Figure 9), centred in the z direction, the results for the pattern along the aperture of the horn, in comparison to those from the analytical solution are generated in Figure 10. The patterns from the TLM models will never match the analytical solution directly due to the stepwise nature of the computation space. The boundaries are placed at the ends of the transmission lines of length $\Delta x/2$, in comparison to some TLM models which place the boundary at the node. A section of wave-guide of length 150 nodes is appended to the beginning of the model to ensure any errors from the PML have little effect on the signal propagating into the horn. This approach is also used in the BMH and uniform models. A mean error (sum of absolute differences) of 0.0583 is observed, indicating that while the technique produces considerably accurate results given the simplicity of the formulation, they are far from perfect.

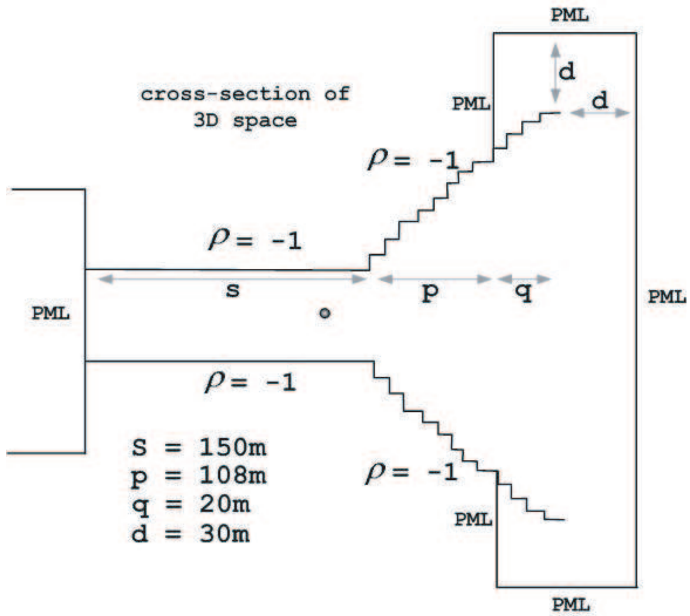

Figure 9: North-south, east-west plane view of 3D E-plane sectoral horn antenna, illustrating TLM stepped formulation.

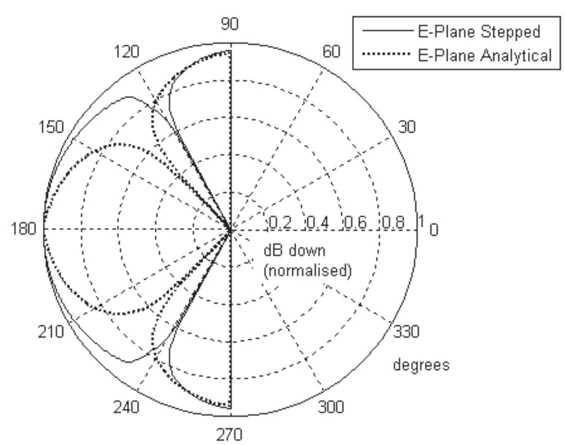

Figure 10: E-plane radiation pattern of E-plane sectoral horn antenna, analytical against stepped TLM (run for 2500 iterations).

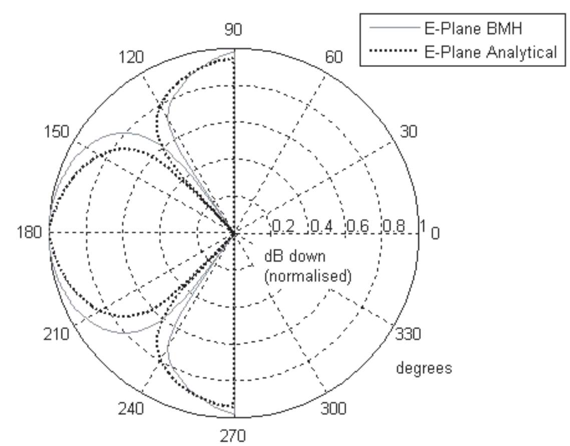

Figure 11: E-plane radiation pattern of E-plane sectoral horn antenna, analytical solution against BMH TLM (run for 788 iterations).

The boundary conforming mesh described in [7] and analysed above was implemented as a comparison to the stepped mesh, again, placing the mouth of the horn inside the computation space, the results which were produced were a considerable improvement on those generated from the stepped mesh and are illustrated in

Figure 11, this is modelled with a reflection coefficient of -1 (or electric wall in the terminology of [7]). As can also be seen the BMH technique requires considerably less iterations than those of the stepped formulation, producing results comparable with the analytical solution after only 788 iterations. The mean error recorded for this mesh was 0.0441.

When the technique that we propose here is implemented, it is clear that its memory requirements are almost identical to those of the stepped mesh. The extra computation needed at the start of the simulation to calculate the lengths of the transmission line segments meeting with the boundaries are usually performed in stepped schemes before the rounding up or down is performed, therefore the only extra computation required in the formulation is the adjustment of the impedances saved in the boundary locations of the impedance matrices. The algorithm then runs in an identical manner to the stepped system. The results produced when this technique was implemented are given in figure 12. The mean error was recorded at 0.0406. Figure 13 shows the uniform scheme in comparison to the BMH results and these are within 0.0035 units of one another, illustrating the accuracy of the new scheme with a substantially smaller computational 'footprint' than the BMH approach.

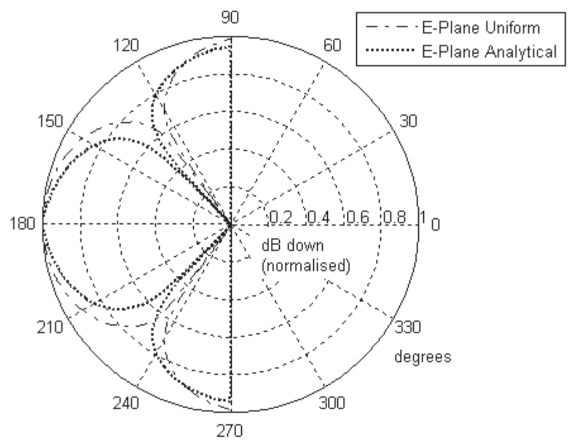

Figure 12: E-plane radiation pattern of E-plane sectoral horn antenna, analytical solution against uniform (run for 2118 iterations).

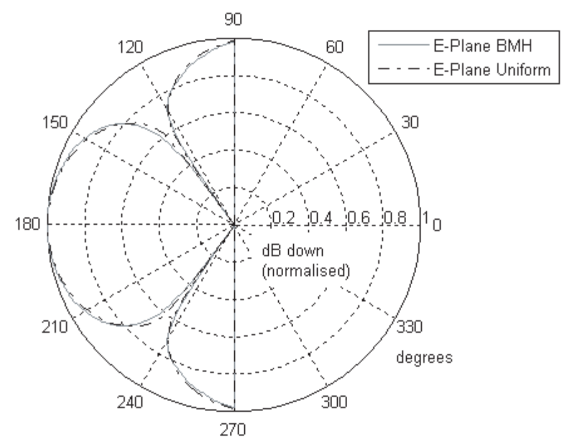

Figure 13: E-plane radiation pattern of E-plane sectoral horn antenna, BMH TLM solution against uniform TLM (BMH run for 788 iterations, uniform run for 2118 iterations).

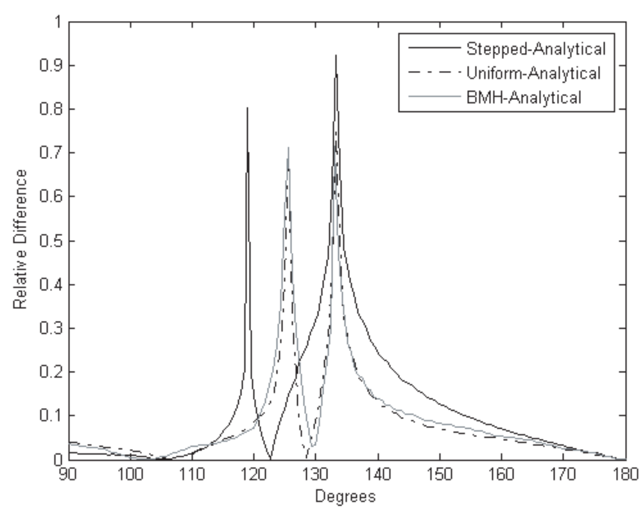

Figure 14: Difference plots of stepped, BMH and uniform TLM models against analytical solution.

Figure 14 gives a graphical view of how close the BMH and uniform models are. Due to the symmetry of the patterns, only half of the plot is shown. As can be observed, the uniform mesh is slightly closer to the analytical solution than the BMH model, while the stepped mesh, as expected, displays significant deviation.

5. Conclusion

The TLM numerical method is widely used, not only in electromagnetics, but many other fields of physics. The technique proposed in this paper gives an accurate approximation to arbitrary placed boundaries of a TLM mesh, while achieving a computational complexity and load equivalent to a normal Cartesian stepped formulation. The method has been compared with another widely used boundary smoothing scheme, illustrating its desirable properties further. The accuracy obtained from the new scheme is in tier with the previously used technique.

We propose this novel approach to model arbitrary placed boundaries of a TLM mesh that do not fall within the discretised formulation of the model. Due to the simplicity of the impedance transformations the computational requirements are practically unaltered from the stepped formulation most commonly used by engineers.

Acknowledgement

The authors would like to acknowledge the assistance and many useful comments which have been provided by Dr. J. Flint, Loughborough University, UK.

REFERENCES

1. Peña, N. and M. M. Ney, "Absorbing-boundary conditions using perfectly-matched-layer (PML) technique for three-dimensional TLM simulations," *IEEE Trans. on Microwave Theory and Techniques*, Vol. MTT-45, 1749–1755, 1997.
2. Tang, T.-W., C. Chrisopoulos, and J. Paul, "Implementation of the stretched co-ordinate based PML for waveguide structures in TLM," *Int. Jnl. of Numerical Modelling*, Vol. 18, 107–118, 2004.
3. De Cogan, D., W. J. O'Connor, and S. Pulko, "Transmission line matrix modelling in computational mechanics," Taylor and Francis/CRC Press, Boca-Raton, 2006.
4. De Cogan, D. and A. de Cogan, "Numerical modelling for engineers", Oxford University Press, 1997.
5. Kreyszig, E., "Advanced engineering mathematics", John Wiley and Sons Inc, Chichester, 1999.
6. Jaycocks, R. and S. Pomeroy, "First international workshop on transmission line matrix (TLM) modelling-theory and applications," University of Victoria, British Columbia (Canada), 269–272, 1–3 August 1995.
7. Mueller, U., A. Beyer, and W. J. R. Hoefer, "Moving boundaries in 2-D and 3-D TLM simulations realized by recursive formulas," *IEEE Trans. on Micro. Theo. and Tech.*, Vol. 40, No. 12, 2267–2271, December 1992.
8. Balanis, C. A., "Antenna theory analysis and design", Harpers and Row Inc, New York, 1982.

A Fast Matlab-based 3D Finite Difference Frequency Domain (FDFD) Method and Its Application to Subsurface Scatterers

Q. Z. Dong and C. Rappaport
Northeastern University, USA

The FDFD electromagnetic model computes wave scattering by directly discretizing Maxwell's equations along with specifying the material characteristics in the scattering volume. No boundary conditions are need except for the outer grid termination absorbing boundary. We use a sparse matrix Matlab code with generalized minimum residue (GMRES) Krylov subspace iterative method to solve the large sparse matrix equation, along with the Perfectly Matched Layer (PML) absorbing boundary condition. The PML conductivity profile employs the empirical optimal value from [1–3].

The sparse Matlab-based model is about 100 times faster than a previous Fortran-based code implemented on the same Alpha-class supercomputer. The 3D FDFD model is easily manipulated; it can handle all types of layer-based geometries if the target region is less than 25% of the total computational space.

Several cases have been investigated. The scattered electromagnetic fields due to spherical and elliptic mine-like TNT targets buried in simulated Bosnian soil are computed and compared to reference solutions. The electric field distribution of a cylindrical air void in soil is computed and compared with analytical models. Multiple buried scatterer problems are easily specified and analyzed with FDFD. This method is particularly well-suited to rough surface and volumetric inhomogeneity applications.

REFERENCES

1. Marengo, E., C. Rappaport, and E. Miller, "Optimum PML ABC conductivity profile in FDFD," *IEEE Transactions on Magnetics*, Vol. 35, 1506–1509, 1999.
2. Winton, S. and C. Rappaport, "Specifying PML conductivities by considering numerical reflection dependencies," *IEEE Transactions on Antennas and Propagation*, Vol. 48, No. 7, 1055–1063, July 2000.
3. Rappaport, C., M. Kilmer, and E. Miller, "Accuracy considerations in using the PML ABC with FDFD Helmholtz equation computation," *Int. J. Numer. Modeling*, Vol. 13, 471–482, Sept. 2001.

Modeling Electromagnetic Scattering from Particles

M. J. Berg, **C. M. Sorensen**, **A. Chakrabarti**, **and M. I. Mishchenk**
Kansas State University, USA

Particles of both spherical and nonspherical shape are often encountered in the natural environ- ment. Examples include atmospheric clouds and aerosols. Light scattering from these particles creates radiative forcing effects that influence the Earth's climate [1]. Additionally, electromagnetic scattering from a particle can provide information about the physical properties of the particle in an unintrusive manner. Furthermore, applications of electromagnetic scattering to remote sensing of physical systems of single or multiple particles requires a detailed knowledge of the interaction between the particle and the field. We apply the Discrete Dipole Approximation (DDA) to study electromagnetic scattering from single spherical and nonspherical particles. Our aim is to quantify simple patterns in the scattering process which aid in characterizing the physical properties of a scattering particle [2, 3]. We also examine in detail how an electromagnetic field interacts with a particle at the microscopic level to establish the macroscopic scattering, absorption and extinction cross sections.

REFERENCES

1. Mishchenko, M. I., "Scattering, absorption, and emission of light by small particles," Cambridge, 2002.
2. Sorensen, C. M. and D. J. Fischbach, "Patterns in mie scattering," *Opt. Commun.*, Vol. 173, 145–153, 2000.
3. Berg, M. J., C. M. Sorensen, and A. Chakrabarti, "Patterns in mie scattering: evolution when normalized by the rayleigh cross section," *Appl. Opt.*, In Press, 2005.

The Spectral Expansion on the Entire Real Line of Green's Function for a Three-layer Medium in the Fundamental Functions of a Nonself-adjoint Sturm-Liouville Operator

E. G. Saltykov
Lomonosov Moscow State University, Russian Federation

Abstract—We obtain a new representation for Green's function in the space R^2 of the Helmholtz equation with the coefficient representing a complex-valued piecewise constant function. We set that the coefficient in the equation depends on the one variable and represents three complex constants.

This representation is the expansion of Green's function in the fundamental functions which are bounded on the entire real line R^1 solutions of the ordinary Sturm-Liouville equations with complex coefficients.

The spectrum consists of two half-lines parallel to the real axis on the complex plane, issuing from the points characterized by the coefficient in the equation on semi-infinite intervals, and going in the positive direction of the real axis.

1. Introduction

In the present paper, we obtain a new representation ([1, 2]) for the solution of a problem for a three-layer medium similar to the problem on a dipole in the space containg a plane interface between two media characterized by constant wave numbers $k_i, i = 1, 2$. The latter problem was considered in [3].

The new representation follows from the representation of Green's function in the form of a Fourier integral obtained by reducing an integral on the complex plane of the spectral parameter to integrals over the edges of cuts passing through the points k_i, $i = 0, 2 (k_i = const)$ characterized by the coefficient $k(z)$ of the equation outside a finite interval $[0, H]$ where $k(z) = k_l = const (l = 1)$. The function $k(z)$ represents a complex-valued piecewise constant function of a variable z on the entire real line R^1.

2. Formulations and Equations

Green's function $u(z, x)$ satisfies the Helmholz equation

$$\frac{\partial^2 u}{\partial z^2} + \frac{\partial^2 u}{\partial x^2} + k^2(z)u = -2\delta(z - z')\delta(x - x') \tag{1}$$

with the delta function on the right-hand side and with either the radiation condition $u \to 0$ as $r = \sqrt{z^2 + x^2} \to \infty$ [if $Im\, k(z) \neq 0$] or the radiation condition following from the limiting absorption principle [if $Imk(z) = 0$]. The function u is a bounded function in R^2 with the exception of the source position $M'(z', x')$ where it has a logarithmic singularity. At the points $z = 0, z = H$ of discontinuity of the function $k(z)$, the function $u(z, x)$ satisfies the matching conditions for the function and its normal derivative on the boundary. We consider Eq. (1)under the assumption that $z, z', x, x' \in R^1$, where R^1 is the real axis. We set

$$k(z) = \begin{cases} k_0 = const, z < 0, \\ k_1 = const, 0 < z < H, \\ k_2 = const, z > H. \end{cases}$$

where the k_l are complex constants, $k_l^2 = \varepsilon_l + j\sigma_l$, $\varepsilon_l \in R^1$, $\varepsilon_0 = \varepsilon_2, \sigma_l \geq 0$, $\sigma_0 < \sigma_1 < \sigma_2$ or $\sigma_0 > \sigma_1 > \sigma_2$, $l = 0, 1, 2$, and j is the imaginary unit.

To find the solution, we consider the Fourier expansion of u with respect to the variable x [of which the cofficient in Eq. (1) is independent]:

$$u = \lim_{\Lambda \to \infty} u_\Lambda, \qquad u_\Lambda = \frac{1}{\pi} \int_{-\Lambda}^{\Lambda} e^{j\alpha(x - x')} g(z, z'; \alpha)\, d\alpha. \tag{2}$$

The function g can be found from the equation

$$lg + \alpha^2 g = \delta(z - z'), \qquad z, z' \in R^1, \tag{3}$$

where l is the differential operator

$$l\psi = -d^2\psi/dz^2 - k^2(z)\psi,$$

and has the form

$$g(z, z'; \alpha) = \frac{\psi(z_>, \alpha)\varphi(z_<, \alpha)}{w(\alpha)}. \tag{4}$$

Here $z_> = max(z, z')$, $z_< = min(z, z')$, and $w(\alpha)$ is the Wronskian of the linearly independent solutions ψ and φ of the homogeneous Eq. (3). The function g is bounded for $z, z' \in R^1$ and satisfies the matching condition for the function and its derivative dg/dz at the points $z = 0$ and $z = H$.

Taking into account the representation (4) of the function g via the functions φ, ψ, and w, we find that the function g has the ramification points $\pm k_i$ in the complex plan α ([4] p. 23–25, Vol. 2 of the Russian translation).

The cuts corresponding to the ramification points k_i go along the lines

$$\alpha = \sqrt{-\mu^2 + k_i^2} = j\sqrt{\mu^2 - k_i^2}, \qquad \mu \in R^1,\ i = 0, 2.$$

We assume that $Re\sqrt{-\mu^2 + k_i^2} \geq 0$, and $Re\sqrt{\mu^2 - k_i^2} \geq 0$.

Consider the case in which $\varepsilon_0 = \varepsilon_2$, $\sigma_2 > \sigma_0$, $\sigma_0 > 0$, $\sigma_2 > \sigma_1 > \sigma_0$.

The Wronskian $w(\alpha) \neq 0$ on the entire complex α-plane [5, 6].

Consider the case $x - x' > 0$.

Using the Cauchy theorem, we reduce the integral u_Λ given by (2) in the upper half of the complex α-plane to two integrals over the edges of the cuts passing through the points k_i and the integral I_{C_Λ} over the half-circle C_Λ of the radius Λ.

We have

$$u_\Lambda(z, x) = \sigma_\Lambda(z, u) + I_{C_\Lambda}, \tag{5}$$

where

$$\sigma_\Lambda(z, u) = \frac{j}{\pi}\sum_{i=0,2}\int_{-M_i(\Lambda)}^{M_i(\Lambda)} \mu \frac{e^{-\sqrt{\mu^2 - k_i^2}(x - x')}}{\sqrt{\mu^2 - k_i^2}} \frac{\psi_i(z_>, \mu)\varphi_i(z_<, \mu)}{w_i(\mu)} d\mu. \tag{6}$$

The function $M_i(\Lambda)$, which define the limits of integration in (6), depend on Λ, and $M_i(\Lambda) \sim \Lambda$ as $\Lambda \to \infty$. The quantity $M_i(\Lambda) > 0$ occuring in (6) is the value of μ at which the right edge of the cut passing through the point k_i intersects the half-circle C_Λ.

The functions $\psi_i(z, \mu)$ and $\varphi_i(z, \mu)$ are linearly independent solutions of the equations

$$l\chi_i = (\mu^2 - k_i^2)\chi_i,\ \mu \in R^1,\ i = 0, 2. \tag{7}$$

They are related to the functions $\psi(z, \alpha)$ and $\varphi(z, \alpha)$ [which are linearly independent solutions of the equation $(l + \alpha^2)\chi = 0$] by the formula $\chi(z, \mu) = \chi(z, \alpha = j(\mu^2 - k_i^2)^{1/2})$.

The Wronskian on the cuts passing through the ramification points k_i is given by the formula $w_i(\mu) = w(\alpha = j(\mu^2 - k_i^2)^{1/2})$.

The integral I_{C_Λ} occuring in (5) has the form

$$I_{C_\Lambda} = \frac{1}{\pi}\int_{C_\Lambda} e^{j\alpha(x - x')} g(z, z'; \alpha) d\alpha,$$

where C_Λ is the half-circle of radius Λ centered at the point $\alpha = 0$ in the upper half-plane of the complex variable α.

We introduce the functions $\eta^l = \sqrt{\alpha^2 - k_l^2}, l = 0, 1, 2, Re\eta^l \geq 0$. The representations of the functions ψ_i, φ_i, and w_i can be derived from ψ, φ, and w with regard to the the fact that $Im\eta^l < 0$ in the domain lying on the left of the hyperbola $\alpha_2 = \sigma_l/(2\alpha_1)$ passing through the point k_l in the upper half-plane of the variable $\alpha = \alpha_1 + j\alpha_2$; next, $Im\eta^l > 0$ in the domain on the right of the hyperbola $\alpha_2 = \sigma_l/(2\alpha_1)$ passing through the point k_l ([4] p. 30, Vol.2 of the Russian translation). The following condition is satisfied on the cuts drawn along the hyperbolas: $\mu > 0$ on the right edge of the cut, and $\mu < 0$ on the left edge of the cut passing trough the points k_i, i=0, 2.

We have $I_{C_\Lambda} \to 0$ as $\Lambda \to \infty$.

Using the functions $u_0 = \psi_0$ and $u_2 = \varphi_2$, we can rewrite the function (6) as

$$\sigma_\Lambda(z, u) = \sum_{i=0,2}\int_0^{M_i(\Lambda)} \frac{e^{-\sqrt{\mu^2 - k_i^2}(x - x')}}{\sqrt{\mu^2 - k_i^2}} u_i(z, \mu)u_i(z', \mu)dp_i(\mu), \tag{8}$$

where $dp_0(\mu) = d\mu/a_0^0(\mu)b_0^0(\mu)2\pi$, $dp_2(\mu) = d\mu/a_2^2(\mu)b_2^2(\mu)2\pi$. a_i^i and b_i^i are coefficients connected with transmission and reflection coefficients of u_i.

In deriving (8), we represent the integral (6) as two integrals over the positive and negative semiaxis and make the change of variables $\mu' = -\mu$ in the integral over the negative semiaxis.

Passing to the limit in (5) as $\Lambda \to \infty$, we obtain the representation

$$u = \sum_{i=0,2} \int_0^\infty \frac{e^{-\sqrt{\mu^2-k_i^2}(x-x')}}{\sqrt{\mu^2-k_i^2}} u_i(z,\mu) u_i(z',\mu) dp_i(\mu). \tag{9}$$

which holds for $x - x' > 0$.

In a similar way, we consider the case $x - x' < 0$ by reducing the integral u_Λ with the use of the Cauchy theorem in the lower half-plane of the complex variable α to two integral over the edges of the cuts passing through the points $-k_i$.

Passing to the limit in (9) as $x \to x'$, we obtain relation (9)) with $x = x'$.

3. Conclusion

We have thereby obtained the definitive representation

$$u = \sum_{i=0,2} \int_0^\infty \frac{e^{-\sqrt{\mu^2-k_i^2}|x-x'|}}{\sqrt{\mu^2-k_i^2}} u_i(z,\mu) u_i(z',\mu) dp_i(\mu), \tag{10}$$

which is valid for $x, x'z, z' \in R^1$. This representation of Green's function u was obtained under the assumption that $\sigma_2 > \sigma_0 > 0\,(\sigma_2 > \sigma_1 > \sigma_0)$ The case $0 < \sigma_2 < \sigma_0\,(\sigma_2 < \sigma_1 < \sigma_0)$ can be treated in a similar way.

The representation (10) is the expansion of Green's function in the fundamental functions u_i, which are bounded on the entire real line R^1 solutions of the ordinary Sturm-Liouville Eq. (7) with complex coefficients. This expansion is characterized by the spectral measure, which is a diagonal matrix function with nonzero entries $p_i(\mu)$.

Equation (7) for the functions u_i indicates that the spectrum $\lambda = \mu^2 - k_i^2$, $\mu \in R^1$, consists of two half-lines parallel to the real axis on the complex λ-plane, issuing from the points $-k_i^2$, and going in the positive direction of the real axis.

Passing to the limit as $\sigma_2 \to \sigma_0$, we arrive the case $\sigma_0 = \sigma_2$.

If $\sigma_2 \to 0$ and $\sigma_0 \to 0$, then we obtain the limit case $\sigma_0 = \sigma_2 = 0$. Then the spectrum belongs to real axis, and the spectrum is double for $\lambda \geq -\varepsilon_0$. In this case, the lower bound of the spectrum is limited to the number $\lambda = -\varepsilon_0$. This case is an example of the expansion of a function of the class $L_p(R^1), p > 2$, in the fundamental functions of the Sturm-Liouville operator with a real coefficient $-k^2(z)$ satisfying the Kato condition ([7]).

Acknowledgment

The author is grateful to V. A. Ilín for permanent attention and support of the research and V.I. Dmitriev for his interest in this work and the suggestion that the singularities of the function g given by (3) similar to ramification points should be related to the expansion of Green's function in the fundamental functions of the operator l.

REFERENCES

1. Dmitriev, V. I. and E. G. Saltykov, "The new representation of Green's function of Sommerfeld's problem for a conductive homogeneous half-space," *Uspekhi Mat. Nauk* , Vol. 49, No. 4(298), 79–80, 1994.
2. Saltykov, E. G., "The spectral expansion on the entire real line of Green's function for two-layer medium in the eigenfunctions of a nonself-adjoint Sturm-Liouville operator," *Differents. Uravn.*, Vol. 38, No. 5, 687–691, 2002.
3. Sommerfeld, A., *Differentialgleichungen der Physik, Db. VI*, Leipzig, 1948. Translated under the title *Differentsialńye Uravneniya v Chastnykh Proizvodnykh Fiziki*, 358, Inostrannaya Literatura, Moscow, 1950.
4. Felsen, L. and N. Marcuvitz, *Radiation and Scattering of Waves*, Prentice-Hall, Englewood Cliffs, 1973. Translated under the title *Izluchenie i Rasseyanie Voln*, Moscow, 1978.
5. Saltykov, E. G., "Absence of poles in integrand of Green's function for a three-layer medium," *PIERS 2005 Progress In Electromagnetic Research Symposium, Abstracts*, 183, Hangzhou, China, 2005.
6. Dmitriev, V. I. and E. G. Saltykov, "Absense of poles in integrand of the Green's function for special model of three layers medium," *International conference "Differantial Equations and Related Topics"*, 111, Moscow, 2001.
7. Ilín, V. A., "Uniform equiconvergence of the spectral expansion corresponding to a self-adjoint extension of the Schrödinger operator with a uniformly locally integrable potential with the Fourier integral on the entire axis R," *Differents. Uravn.*, Vol. 31, No. 12, 1957–1967, 1995.

Simulation of Electromagnetic Fields of Electromagnetic in Separator

X. F. Tan
Hunan Institute of Science and Technology, China

Electromagnetic Separator are high performance devices utilizing a powerful magnetic force for separation of magnetic foreign matter form raw material. Electromagnetic Separator is widely applied to metallurgical industry, mining industry, power industry, seaports, cement and construction material. Even in the developing industry jof garbage disposal, the separator is used to recover the iron and steel materials mixed in the scrap stock. The finite element program generating system FEPG is one of finite element method software, which can generate source program. Magnetic potential and magnetic density of magnetic field of Electromagnetic Separator have been studied. The results could help us to know the principle of Electromagnetic Separator well. However, there is still boundary condition and singularity treatment and large matrix cost in the FEM method. These historic difficult are overcame by AGILD and GL method. Recently Hunan KMD electrical company used GL geophysical Laboratory's AGILD and GL parallel electromagnetic modeling method for KMD stirring electromagnetic field simulation and obtained excellent result and obtained dynamic rotation magnetic imaging first in the world. We will use AGILD modeling for our Separator simulation

REFERENCES

1. Xie, G. Q., J. Li, and J. H. Li, "New AGILD EMS electromagnetic field Modeling," *Progress In Electromagnetics Research Symposium 2005*, Hangzhou, China, August 22-26, 2005.
2. Xie, G. Q., J. H. Li, E. Majer, D. Zuo, and M. Oristaglio, "3-D electromagnetic modeling and nonlinear inversion," *Geophysics*, Vol. 65, No. 3, 804, 2000.